
Hierarchical Refinement: Optimal Transport to Infinity and Beyond

Peter Halmos^{1*} Julian Gold^{2*} Xinhao Liu¹ Benjamin J. Raphael¹

Abstract

Optimal transport (OT) has enjoyed great success in machine-learning as a principled way to align datasets via a least-cost correspondence. This success was driven in large part by the runtime efficiency of the Sinkhorn algorithm (Cuturi, 2013), which computes a coupling between points from two datasets. However, Sinkhorn has quadratic space complexity in the number of points, limiting the scalability to larger datasets. Low-rank OT achieves linear-space complexity, but by definition, cannot compute a one-to-one correspondence between points. When the optimal transport problem is an assignment problem between datasets then the optimal mapping, known as the *Monge map*, is guaranteed to be a bijection. In this setting, we show that the factors of an optimal low-rank coupling co-cluster each point with its image under the Monge map. We leverage this invariant to derive an algorithm, *Hierarchical Refinement* (HiRef), that dynamically constructs a multiscale partition of a dataset using low-rank OT subproblems, culminating in a bijective coupling. Hierarchical Refinement uses linear space and has log-linear runtime, retaining the space advantage of low-rank OT while overcoming its limited resolution. We demonstrate the advantages of Hierarchical Refinement on several datasets, including ones containing over a million points, scaling full-rank OT to problems previously beyond Sinkhorn’s reach.

1. Introduction

Optimal transport (OT) is a mathematical framework for comparing probability distributions μ and ν . Given a cost function c , the *Monge* formulation of the OT problem is to find a mapping T transforming a distribution μ into ν

(i.e. $T_{\#}\mu = \nu$) with least-cost. A relaxation of this problem, called the *Kantorovich* formulation, instead computes a least-cost coupling γ between μ and ν . The Kantorovich formulation allows mass splitting and thus a solution always exists; in contrast, a Monge map between μ and ν may not exist. When a Monge map T does exist, the solution to the Kantorovich problem is a coupling $\gamma = (\text{id} \times T)_{\#}\mu$ supported on its graph, and the Monge and Kantorovich problems coincide (Brenier, 1991).

When μ and ν are discrete uniform measures on n points the optimal transport problem reduces to an assignment problem. Classical algorithms such as the Hungarian algorithm and Network Simplex (Tarjan, 1997; Orlin, 1997), solve this in cubic time. The Sinkhorn algorithm (Cuturi, 2013) solves the entropy-regularized Kantorovich problem with quadratic runtime, greatly expanding the applicability of computational OT. However, the Sinkhorn algorithm requires quadratic space to store the coupling γ .

In the past several years, OT has found numerous applications in machine learning and across science, including: domain adaptation (Courty et al., 2014; Solomon et al., 2015), self-attention (Tay et al., 2020; Sander et al., 2022; Geshkovski et al., 2023), computational biology (Schiebinger et al., 2019; Yang et al., 2020; Zeira et al., 2022; Bunne et al., 2023; Halmos et al., 2025b; Klein et al., 2025), unpaired data translation (Korotin et al., 2021; De Bortoli et al., 2024; Tong et al., 2024; Klein et al., 2024), and alignment problems in transformers and large language models (Melnyk et al., 2024; Li et al., 2024). The *least-cost* principle of optimal transport is crucial for training high-quality generative models using Schrödinger bridges, flow-matching, diffusion models, or neural ordinary differential equations (Finlay et al., 2020; Tong et al., 2023; De Bortoli et al., 2024; Kornilov et al., 2024; Klein et al., 2024). These models typically require millions to hundreds of millions of data-points to achieve high-performance at scale (Ramesh et al., 2021), limiting the scope of OT for generative modeling.

As modern datasets grow to have tens of thousands or even millions of points, the quadratic space and time complexity of Sinkhorn becomes increasingly prohibitive. This limitation is widely recognized in the machine learning literature, with (De Bortoli et al., 2024) noting that the quadratic complexity of optimal transport renders its application to modern

^{*}Equal contribution ¹Department of Computer Science, Princeton University ²Center for Statistics and Machine Learning, Princeton University. Correspondence to: Benjamin J. Raphael <braphael@princeton.edu>.

datasets on the order of millions of points impractical. A number of approaches have been proposed to address scaling OT to massive datasets which avoid instantiation of a full coupling matrix. Mini-batch OT (Genevay et al., 2018) improves scalability, but incurs significant biases (Sommerfeld et al., 2019; Korotin et al., 2021; Fatras et al., 2021) as each mini-batch alignment is a poor representation of the global one. Neural optimal transport methods (Makkuva et al., 2020; Bunne et al., 2023; Fan et al., 2023; Korotin et al., 2023; Buzun et al., 2024), parametrize the Monge map as a deterministic neural network rather than materializing a quadratic coupling matrix. However, these methods have noted limitations recovering faithful maps (Korotin et al., 2021). Other methods (De Bortoli et al., 2021; De Bortoli et al., 2024) solve for a *stochastic* map through the Schrödinger bridge problem, but do not solve the primal optimal transport problem directly.

Another approach to improve space complexity of OT is to introduce a *low-rank* constraint on the coupling matrix in the Kantorovich problem. This has been done by parameterizing the coupling through a set of low-rank factors (Scetbon et al., 2021; 2022; Scetbon & Cuturi, 2022; Scetbon et al., 2023; Halmos et al., 2024) or by using a proxy objective for the low-rank problem, factoring the transport through a small number of anchor points (Forrow et al., 2019; Lin et al., 2021). For a given rank r these approaches have $O(nr)$ space complexity, enabling *linear* space scaling. Low-rank OT has been used successfully on datasets on the order of 10^5 samples with ranks on the order of 10^1 (Scetbon et al., 2023; Halmos et al., 2024; 2025a; Klein et al., 2025), but computing *full-rank* couplings between datasets of sizes on the order of 10^5 and greater has not yet been accomplished.

Contributions. We introduce Hierarchical Refinement (HiRef), an algorithm to scalably compute a full-rank alignment between two equally-sized input datasets X and Y by solving a hierarchy of low-rank OT sub-problems. The success of this refinement is driven by a theoretical result, Proposition 3.1 below, stating that factors of an optimal low-rank coupling between X and Y co-cluster points X with their image under the Monge map $T(X) = Y$. We leverage Proposition 3.1 recursively to obtain increasingly fine partitions of X and Y . At each scale, the solutions to low-rank OT sub-problems are bijective (and thus full-rank) correspondences between the partitions of X and Y . Iterating to the finest scale gives a bijection between X and Y .

Hierarchical Refinement constructs a *multiscale partition* of each dataset, and thus is related to (Gerber & Maggioni, 2017), which introduced a general framework for multiscale optimal transport using such partitions, as well as the earlier work of (Mérigot, 2011). Unlike (Mérigot, 2011; Gerber & Maggioni, 2017), Hierarchical Refinement (i) does not assume multiscale partitions for each dataset are given, instead constructing them on the fly; and (ii) operates intrinsically

to the data, not relying on a mesh or anchor points in the ambient space of the data, avoiding the curse of dimensionality.

We demonstrate that Hierarchical Refinement computes OT maps efficiently in high-dimensional spaces, often matching or even outperforming Sinkhorn in terms of primal cost. Moreover, HiRef has linear space complexity and time complexity scaling log-linearly in the dataset size. Unlike low-rank OT, Hierarchical Refinement places X and Y in bijective correspondence. Hierarchical Refinement scales to over a million points, enabling the use of OT on massive datasets without incurring the bias of mini-batching.

2. Background and Related Work

Suppose $X = \{\mathbf{x}_i\}_{i=1}^n$ and $Y = \{\mathbf{y}_j\}_{j=1}^m$ are datasets in the same metric space $(\mathcal{X}, d_{\mathcal{X}})$. Let $c : \mathcal{X} \times \mathcal{X} \rightarrow \mathbb{R}_+$ be a cost function. This cost c is often assumed to satisfy strict convexity or to be a metric. Datasets X and Y are represented as discretely supported probability measures $\mu = \sum_{i=1}^n \mathbf{a}_i \delta_{\mathbf{x}_i}$ and $\nu = \sum_{j=1}^m \mathbf{b}_j \delta_{\mathbf{y}_j}$ for probability vectors $\mathbf{a} \in \Delta_n$ and $\mathbf{b} \in \Delta_m$.

Monge Problem Optimal transport has its origin in the *Monge problem* (Monge, 1781), concerned with finding an optimal map $T : X \rightarrow Y$ pushing μ forward to ν :

$$M_c(\mu, \nu) = \min_{T: T_{\#}\mu = \nu} \mathbb{E}_{\mu} c(x, T(x)). \quad (1)$$

Above, $T_{\#}\mu$ denotes the pushforward of μ under T , defined as the measure on Y with $T_{\#}\mu(B) := \mu(T^{-1}(B))$ for any (measurable) set $B \subset Y$. In general, a Monge map may not exist (e.g. when $m > n$). However, when $|X| = |Y| = n$ and \mathbf{a}, \mathbf{b} are uniform then the Monge problem becomes the *assignment problem* and has a solution (Thorpe, 2017). These solutions correspond to bijections between X and Y .

Kantorovich Problem The *Kantorovich problem* (Kantorovich, 1942) was introduced as a relaxation of the Monge problem. In contrast to the Monge problem, the Kantorovich problem allows mass-splitting and a solution is always guaranteed to exist. Define the *transport polytope* $\Pi_{\mathbf{a}, \mathbf{b}}$ as the following set of coupling matrices

$$\Pi_{\mathbf{a}, \mathbf{b}} := \{\mathbf{P} \in \mathbb{R}_+^{n \times m} : \mathbf{P} \mathbf{1}_m = \mathbf{a}, \mathbf{P}^T \mathbf{1}_n = \mathbf{b}\}, \quad (2)$$

respectively with left (or “source”) marginal \mathbf{a} and with right (or “target”) marginal \mathbf{b} . For the cost $c(\cdot, \cdot)$, define the cost matrix \mathbf{C} by $\mathbf{C}_{ij} = c(x_i, y_j)$. In this discrete setting, the Kantorovich problem seeks a least cost coupling matrix $\mathbf{P} \in \Pi(\mathbf{a}, \mathbf{b})$ between the probability vectors \mathbf{a}, \mathbf{b} associated to each measure μ, ν :

$$W_c(\mu, \nu) = \min_{\mathbf{P} \in \Pi(\mathbf{a}, \mathbf{b})} \langle \mathbf{C}, \mathbf{P} \rangle_F. \quad (3)$$

The optimal value $W_c(\mu, \nu)$ of (3) is called the c -Wasserstein distance between μ and ν .

Sinkhorn Algorithm and the ϵ -schedule. The Sinkhorn algorithm (Cuturi, 2013) relaxes the classical linear-programming formulation of optimal transport by solving an entropy regularized version of (3),

$$W_\epsilon(\mu, \nu) := \min_{\mathbf{P} \in \Pi_{\mathbf{a}, \mathbf{b}}} \langle \mathbf{C}, \mathbf{P} \rangle_F - \epsilon H(\mathbf{P}), \quad (4)$$

where $H(\mathbf{P}) := -\sum_{ij} \mathbf{P}_{ij} (\log \mathbf{P}_{ij} - 1)$ is the Shannon entropy, and the parameter $\epsilon > 0$ is the regularization strength. The Sinkhorn algorithm improved the $O(n^3 \log n)$ time complexity of classical techniques used for OT such as the Hungarian algorithm (Kuhn, 1955) and Network Simplex (Orlin, 1997; Tarjan, 1997) to $O(n^2 \log n)$ (Luo et al., 2023). As $\epsilon \downarrow 0$, the optimal plan $\mathbf{P}^{*, \epsilon}$ for (4) converges to sparse optimal plan for (3) at an extremal point of the transport polytope (c.f. (Peyré et al., 2019)). However, the number of iterations required scales as $\text{poly}(1/\epsilon)$, diverging as ϵ decreases.

A technique used to improve this scaling is the ϵ -schedule, an adaptive, step-dependent set of entropy parameters $(\epsilon_t)_{t=1}^{t_{\text{fin}}}$ which is monotone-decreasing $\epsilon_1 > \epsilon_2 > \dots > \epsilon_{t_{\text{fin}}}$. As ϵ corresponds to a temperature parameter in the Sinkhorn factorization $\mathbf{P} = \text{diag}(e^{-\mathbf{f}/\epsilon}) e^{-\mathbf{C}/\epsilon} \text{diag}(e^{-\mathbf{h}/\epsilon})$ (Cuturi, 2013; Sinkhorn, 1966), this *annealing* from high-temperature (high ϵ) to low-temperature (low ϵ) gradually drives a dense initial condition to a sparser solution with a faster $\log(1/\epsilon)$ rate (Chen et al., 2023).

Low-rank Optimal Transport The nonnegative rank $\text{rk}_+(\mathbf{M})$ of matrix \mathbf{M} is the smallest number of nonnegative rank-1 matrices summing to \mathbf{M} . Let $\Pi_{\mathbf{a}, \mathbf{b}}(r) := \{\mathbf{P} \in \Pi_{\mathbf{a}, \mathbf{b}} : \text{rk}_+(\mathbf{P}) = r\}$ be the set of rank- r couplings. The low-rank Wasserstein problem for general cost matrix \mathbf{C} is:

$$\mathbf{P}^* = \arg \min_{\mathbf{P} \in \Pi_{\mathbf{a}, \mathbf{b}}(r)} \langle \mathbf{C}, \mathbf{P} \rangle_F. \quad (5)$$

From (Cohen & Rothblum, 1993), each $\mathbf{P} \in \Pi_{\mathbf{a}, \mathbf{b}}(r)$ may be decomposed as $\mathbf{P} = \mathbf{Q} \text{diag}(1/\mathbf{g}) \mathbf{R}^T$, where $\mathbf{g} \in \Delta_r$, $\mathbf{Q} \in \Pi_{\mathbf{a}, \mathbf{g}}$ and $\mathbf{R} \in \Pi_{\mathbf{b}, \mathbf{g}}$. This factorization was introduced to optimal transport by (Scetbon et al., 2021) in the context of the general low-rank problem (5). The factors \mathbf{Q} and \mathbf{R} constitute soft co-clusterings of datasets \mathbf{X} and \mathbf{Y} onto the *same* set of r cluster labels. Other factorizations have recently been proposed (Halmos et al., 2024), using \mathbf{Q} , \mathbf{R} and an intermediate latent coupling \mathbf{T} to solve (5).

Multiscale Approaches to OT Building on the semidiscrete approach of (Aurenhammer et al., 1998), (Mérigot, 2011) uses Lloyd’s algorithm to progressively coarse-grain

the target measure, propagating couplings computed between source and coarse-grained target to initialize an optimization at the next scale. More recently, using a regular family of multiscale partitions on *each* dataset (see Definition C.3), (Gerber & Maggioni, 2017) formalize a general hierarchical approach to the Kantorovich problem (3). They propose: (i) solving a Kantorovich problem between the coarsest partitions of \mathbf{X} and \mathbf{Y} in their respective multiscale families; and (ii) propagation of the optimal plan at scale $t \in \{1, \dots, \kappa - 1\}$ to initialize the optimization at scale $t + 1$. They take as input a chain of partitions and measures across scales:

$$\begin{aligned} (\mathbf{X}^{(1)}, \mu_1) &\rightarrow \dots \rightarrow (\mathbf{X}^{(\kappa)}, \mu_\kappa), \\ (\mathbf{Y}^{(1)}, \nu_1) &\rightarrow \dots \rightarrow (\mathbf{Y}^{(\kappa)}, \nu_\kappa), \end{aligned}$$

where each dataset \mathbf{X}, \mathbf{Y} is identified with the trivial partitions $\mathbf{X}^{(\kappa)} = \{\{\mathbf{x}\} : \mathbf{x} \in \mathbf{X}\}$ and $\mathbf{Y}^{(\kappa)} = \{\{\mathbf{y}\} : \mathbf{y} \in \mathbf{Y}\}$. At the finest scale κ , (Gerber & Maggioni, 2017) recover the original datasets and a near optimal plan for (3).

While a naive implementation of this idea still requires quadratic memory complexity, (Gerber & Maggioni, 2017) propose several propagation strategies to mitigate this, following (Glimm & Henscheid, 2013; Oberman & Ruan, 2015; Schmitzer, 2016). These strategies all use the optimal plan at scale t to restrict the support of the plan computed at the next scale.

In particular, the potential refinement strategy employed by (Glimm & Henscheid, 2013) uses the variables in the dual problem to (3) for a local optimality criterion, carefully choosing the support of plans at subsequent scales to ensure optimality of the plan at the finest scale. In a similar spirit, (Schmitzer, 2016) introduced shielding neighborhoods to provide local optimality criteria for discrete OT. These local optimality criteria for discrete OT parallel Brenier’s theorem (Brenier, 1991) in the continuous setting, and in the next section, we give our own such criterion, Proposition 3.1.

3. Methods

3.1. Low-rank optimal transport co-clusters source-target pairs under the Monge map

We first show that under a few modest assumptions, the optimal low-rank factors $(\mathbf{Q}^*, \mathbf{R}^*)$ for a *variant* of the low-rank Wasserstein problem (5) have qualities that are suited to our refinement strategy. Specifically, we parameterize low-rank plans using the factorization $\mathbf{P} = \mathbf{Q} \text{diag}(1/\mathbf{g}) \mathbf{R}^T$ of (Scetbon et al., 2021) of rank- r plan \mathbf{P} , fixing $\mathbf{g} \in \Delta_r$ to be uniform. Define the following variant of (5) :

$$(\mathbf{Q}^*, \mathbf{R}^*) = \arg \min_{\substack{\mathbf{Q} \in \Pi_{\mathbf{a}, \mathbf{g}}, \mathbf{R} \in \Pi_{\mathbf{b}, \mathbf{g}}, \\ \mathbf{g} = \mathbf{1}_r / r}} \langle \mathbf{C}, \mathbf{Q} \text{diag}(1/\mathbf{g}) \mathbf{R}^T \rangle_F. \quad (6)$$

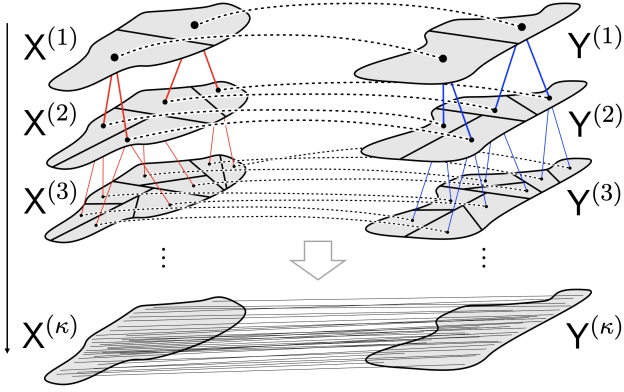


Figure 1. Hierarchical Refinement algorithm: low-rank optimal transport is used to progressively refine partitions at the previous scale, with the coarsest scale partitions denoted $X^{(1)}, Y^{(1)}$, and the finest scale partitions $X^{(\kappa)}, Y^{(\kappa)}$ corresponding to the individual points in the datasets.

We show (Lemma B.1) that optimal Q^* and R^* for (6) correspond to hard-clusterings of each dataset for rank $r = 2$, given by clustering functions

$$q^* : X \rightarrow [2], \quad r^* : Y \rightarrow [2]. \quad (7)$$

The main result underlying Hierarchical Refinement is as follows.

Proposition 3.1 (Optimal low-rank factors co-cluster Monge pairs). *Let $X, Y \subset \mathbb{R}^d$ with $|X| = |Y| = 2^k =: n$, and let $\mathbf{a}, \mathbf{b} \in \Delta_n$ be uniform so that a Monge map $T^* : X \rightarrow Y$ exists. If (Q^*, R^*) are minimizers of (6), with rank $r = 2$ and corresponding clustering functions q^*, r^* as in (7), then for all $\mathbf{x} \in X$:*

$$q^*(\mathbf{x}) = r^* \circ T^*(\mathbf{x}). \quad (8)$$

The proof of this proposition is by contradiction: assume that $\mathbf{x}_i, T^*(\mathbf{x}_i)$ are in different co-clusters according to q^*, r^* , then using cyclical monotonicity, we show that a lower cost can be obtained by a simple rearrangement of the point assignments. The use of cyclical monotonicity echoes the potential refinement strategy of (Glimm & Henscheid, 2013; Gerber & Maggioni, 2017) and the shielding neighborhoods of (Schmitzer, 2016). We note that the assumption that the datasets are of size 2^k is without loss of generality. For a dataset of size n , let $q = \min \{2^t \mid t \in \mathbb{N}, 2^t > n\}$ and add $q - n$ “dummy” points at infinite distance from X, Y , and mutual distance zero.

3.2. Hierarchical Refinement Algorithm

The Hierarchical Refinement algorithm (Algorithm 1) uses Proposition 3.1 to guarantee that each low-rank step co-clusters the datasets optimally, in that \mathbf{x} and $T^*(\mathbf{x})$ are

assigned the same label by q^* and r^* . Using the same label set to partition X and Y automatically places the blocks of each partition in bijective correspondence. One then recurses on each pair of corresponding blocks (which we call a *co-cluster*) at the previous scale, until all blocks have size one. This guarantee holds despite that optimal (Q^*, R^*) for (6) may not constitute an optimal triple $(Q^*, R^*, \mathbf{1}_r/r)$ for the original low-rank problem (5) under the (Scetbon et al., 2021) factorization.

Proposition 3.2. *Given an optimal solver for low-rank couplings, Algorithm 1 generates an optimal full-rank coupling supported on the graph of the Monge map T^* .*

Proof. Applying the invariant of Proposition 3.1 inductively after $\log_2 n$ levels of refinement yields a set of tuples $(\mathbf{x}, T^*(\mathbf{x}))$ containing each $\mathbf{x} \in X$ and its corresponding image $T^*(\mathbf{x})$ under Monge map T^* . \square

Algorithm 1 Hierarchical Refinement

Require: Datasets $X = \{\mathbf{x}_i\}_{i=1}^n, Y = \{\mathbf{y}_i\}_{i=1}^n$; **Low-rank OT solver** $\text{LROT}(\cdot)$; **Rank schedule** $(r_1, r_2, \dots, r_\kappa)$; **Base rank** $r_{\text{base}} = \frac{n}{\prod_{t=1}^{\kappa} r_t}$ (e.g. 1).

Initialize:

```

1:  $t \leftarrow 0, \Gamma_0 \leftarrow \{(X, Y)\}$ 
2: while  $\exists (X^{(t)}, Y^{(t)}) \in \Gamma_t$  with
3:    $\min\{|X^{(t)}|, |Y^{(t)}|\} > r_{\text{base}}$  do
4:    $\Gamma_{t+1} \leftarrow \emptyset$ 
5:   for  $(X_q^{(t)}, Y_q^{(t)}) \in \Gamma_t$  do
6:     if  $\min\{|X_q^{(t)}|, |Y_q^{(t)}|\} \leq r_{\text{base}}$  then
7:        $\Gamma_{t+1} \leftarrow \Gamma_{t+1} \cup \{(X_q^{(t)}, Y_q^{(t)})\}$ 
8:     else
9:        $\mu_{X_q^{(t)}} = \frac{1}{|X_q^{(t)}|} \sum_{\mathbf{x} \in X_q^{(t)}} \delta_{\mathbf{x}}$ 
10:       $\mu_{Y_q^{(t)}} = \frac{1}{|Y_q^{(t)}|} \sum_{\mathbf{y} \in Y_q^{(t)}} \delta_{\mathbf{y}}$ 
11:       $\mathbf{u} \leftarrow \text{UniformInit}(r_{t+1}) \triangleright u_i = 1/r_{t+1}$ 
12:       $(Q, R) \leftarrow \text{LROT}(\mu_{X_q^{(t)}}, \mu_{Y_q^{(t)}}, r_{t+1}, \mathbf{u})$ 
13:      for  $z = 1 \rightarrow r_{t+1}$  do
14:         $X_z^{(t+1)} \leftarrow \text{Select}(X^{(t)}, Q, z)$ 
15:         $Y_z^{(t+1)} \leftarrow \text{Select}(Y^{(t)}, R, z)$ 
16:         $\Gamma_{t+1} \leftarrow \Gamma_{t+1} \cup \{(X_z^{(t+1)}, Y_z^{(t+1)})\}$ 
17:      end for
18:       $\triangleright \text{Select}(S, M, z) = \{s \in S \mid \arg \max_{z'} M_{sz'} = z\}$ 
19:    end if
20:  end for
21:   $t \leftarrow t + 1$ 
22: end while
23: Output:  $\Gamma_t = \{(\mathbf{x}_i, T(\mathbf{x}_i))_{i=1}^n\} \triangleright$  Mapped pairs.
    
```

Thus, assuming that the solver LROT in Algorithm 1 is an optimal low-rank solver for (6), Hierarchical Refinement is guaranteed to return the Monge map.

A hierarchy-depth κ denotes the total number of times Algorithm 1 refines the initial trivial partitions $\{X\}, \{Y\}$. The effective rank at scale t is $\rho_t := \prod_{s=1}^t r_s$, given rank-annealing schedule $(r_1, r_2, \dots, r_\kappa)$ for which ρ_κ divides n . The base rank is $r_{\text{base}} = \frac{n}{\rho_\kappa}$. Note that ρ_t is also the size of each partition at scale t : $\rho_t = |X^{(t)}| = |Y^{(t)}|$, and moreover that this rank-annealing schedule applies to any dataset size n which can be non-trivially factored.

Let $\Gamma_{t,q}$ denote the q -th co-cluster at scale t generated by Hierarchical Refinement:

$$\Gamma_{t,q} := \left\{ (\mathbf{x}, \mathbf{y}) : \mathbf{x} \in X_q^{(t)}, \mathbf{y} \in Y_q^{(t)} \right\}, \quad (9)$$

where $X^{(t)} = \{X_q^{(t)}\}_{q=1}^{\rho_t}$, $Y^{(t)} = \{Y_q^{(t)}\}_{q=1}^{\rho_t}$, and define the co-clustering Γ_t at scale t by:

$$\Gamma_t := \left\{ (X_q^{(t)}, Y_q^{(t)}) \right\}_{q=1}^{\rho_t}.$$

At scale $t \in [\kappa]$, Hierarchical Refinement refines Γ_t to Γ_{t+1} by running a rank r_{t+1} -constrained optimal transport problem between the points in each pair $(X_q^{(t)}, Y_q^{(t)})$ in Γ_t for $q \in [\rho_t]$, yielding factors specific to this $q \in [\rho_t]$:

$$(\mathbf{Q}, \mathbf{R}) \leftarrow \text{LROT}(\mu_{X_q^{(t)}}, \mu_{Y_q^{(t)}}, r_{t+1}, \mathbf{u}_{r_{t+1}}). \quad (10)$$

For each $q \in [\rho_t]$ we use the \mathbf{Q}, \mathbf{R} from (10) to co-cluster $X_q^{(t)}$ with $Y_q^{(t)}$ using r_{t+1} labels. Within this pair, each $\mathbf{x}_i \in X_q^{(t)}$ is assigned a label $z \in [r_{t+1}]$ by taking the argmax over the i -th row of \mathbf{Q} , and likewise each $\mathbf{y}_j \in Y_q^{(t)}$ is assigned the argmax over the j -th row of \mathbf{R} . This is our Select subroutine in Algorithm 1.

The uniform constraint $\mathbf{g} = \mathbf{1}_{r_{t+1}}/r_{t+1}$ in (6) enforces an even split of the dataset, which by Lemma B.1 ensures a partition at optimality (for $r_t = 2$). Repeating for all $q \in [\rho_t]$, one obtains a co-clustering with r_{t+1} components within each co-cluster at the previous scale, leading to a total of $\rho_{t+1} = r_{t+1}\rho_t$ co-clusters at scale $t+1$ (Fig. 1). In practice, we use the low-rank solver (Halmos et al., 2024) to implement Algorithm 1, diagonalizing its output to be of the form $(\mathbf{Q}, \mathbf{R}, \mathbf{g})$, and setting its parameter $\tau_{\text{in}} \uparrow \infty$ to enforce the uniform constraint on \mathbf{g} . If the base-case rank $r_{\text{base}} = 1$, Algorithm 1 returns a collection of n tuples describing a bijection between X and Y .

We emphasize that we do not instantiate the transport plans $\mathbf{P}^{(t)}$ implicit at each scale t ; these ‘‘implicit’’ transport plans may be block-diagonalized, with ρ_t square blocks for each co-clustering, defined by $\mathbf{P}_{ij}^{(t)} := \frac{\rho_t}{n^2} \sum_{q=1}^{\rho_t} \delta_{(\mathbf{x}_i, \mathbf{y}_j) \in \Gamma_{t,q}}$, as discussed in (S8). However, one can still use these plans to define a transport cost $\langle \mathbf{C}, \mathbf{P}^{(t)} \rangle$ at each scale. In Appendix B.4, we show the following bounds on the cost difference across scales.

Proposition 3.3. *Let $c(\cdot, \cdot)$ be a strictly-convex and Lipschitz cost function, let $(r_1, r_2, \dots, r_\kappa)$ be a rank-schedule, and let $\mathbf{P}^{(t)}$ denote the transport plan defined in (S8),*

obtained from step t of Algorithm 1. Define $\Delta_{t,t+1} = \langle \mathbf{C}, \mathbf{P}^{(t)} \rangle_F - \langle \mathbf{C}, \mathbf{P}^{(t+1)} \rangle_F$. Then,

$$0 \leq \Delta_{t,t+1} \leq \|\nabla c\|_\infty \frac{1}{\rho_t} \sum_{q=1}^{\rho_t} \text{diam}(\Gamma_{t,q}), \quad (11)$$

where q indexes co-clusters $\Gamma_{t,q}$ at scale t , defined in (9).

The proof of Proposition 3.3 roughly follows that of Proposition 1 of (Gerber & Maggioni, 2017). In Remark B.5, we discuss how Proposition 3.3 compares, noting that our result makes fewer geometric assumptions on our multiscale partitions $(X^{(t)})_{t=1}^\kappa$ and $(Y^{(t)})_{t=1}^\kappa$ and therefore does not quantify the rate of decay of $\text{diam}(\Gamma_{t,q})$.

3.3. On the Rank-Annealing Schedule

As observed by (Forrow et al., 2019; Scetbon et al., 2021), rank behaves like a temperature parameter: small values of r_i generate coarse partitions of the points, while large values of r_i generate finer partitions. The rank-annealing technique used in Hierarchical Refinement thus parallels the ϵ -schedule, annealing from coarse higher-temperatures $\epsilon \rightarrow \infty$ to fine lower-temperatures $\epsilon \rightarrow 0$ to yield a sparse coupling matrix.

For an integer n , the number of points per sub-problem decays at the rate at which each sub-division occurs, so that Algorithm 1 has log-linear complexity for depth $\kappa = \log n$. However, the large constants required by low-rank OT in practice encourage minimizing the number of calls to LROT as a subroutine, so that if memory permits, it may be advantageous to decrease the depth by storing couplings of higher rank. If desired, memory constraints can be enforced by imposing a maximum rank $r_{\text{max}} \geq r_t$ for all $t \in [\kappa]$ to ensure Hierarchical Refinement only requires $O(nr_{\text{max}})$ space at each step. Thus, we seek factorizations with *minimal* partial sums of ranks while remaining below a desired memory-capacity:

$$\min_{(r_i)_{i=1}^\kappa} \sum_{j=1}^\kappa \rho_j \quad \text{s.t.} \quad \rho_\kappa = n, \quad r_i \leq r_{\text{max}}. \quad (12)$$

The above optimization assumes a base-rank r_{base} of 1; we describe how to handle the general case in Appendix E.1. Importantly, the recursive structure

$$\min_{(r_i)_{i=1}^\kappa} \sum_{j=1}^\kappa \prod_{i=1}^j r_i = \min_{(r_i)_{i=1}^\kappa} \left(r_1 + r_1 \sum_{j=2}^\kappa \prod_{i=2}^j r_i \right) \quad (13)$$

enables a dynamic programming approach to (12), storing a table of factors up to r_{max} to optimize (12) in $O(r_{\text{max}}\kappa n)$ time. Assuming κ, r_{max} are small constants chosen to ensure that all matrices can fit within memory, determining the optimal rank-schedule with respect to $\kappa, n, r_{\text{max}}$ is a simple linear-time procedure.

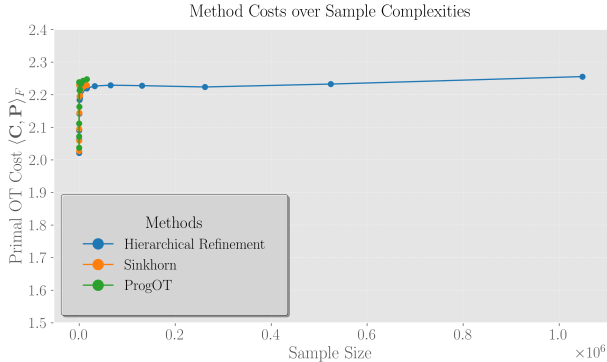


Figure 2. Primal OT cost for varying sample size on the synthetic half-moon S-curve dataset of (Buzun et al., 2024) for HiRef, Sinkhorn, and ProgOT

3.4. Complexity and Scaling of Hierarchical Refinement

For two datasets X, Y of size n , the space complexity of Hierarchical Refinement is $\Theta(n)$, since at each level, one must store Γ_t which is a set of subsets of X and Y . To derive the time-complexity of Hierarchical Refinement, note that if $n = 2^k$, a naive $r = 2$ rank-schedule at each layer requires $\frac{n}{2}$ instances of LROT over rapidly decaying dataset sizes. The complexity of low-rank OT (Scetbon et al., 2021; 2022; Halmos et al., 2024) is linear (Kn) for a large constant $K = O(BLr^2)$ dependent on B the number of inner Sinkhorn iterations, L the number of mirror-descent steps, and $r = \max\{r_1, r_2, d\}$ for r_1, r_2 the ranks of the latent coupling of (Lin et al., 2021; Halmos et al., 2024) and d the rank of a low-rank approximation of cost matrix C . In this setting, the runtime of Algorithm 1 is given by the sum $2^0 O(n) + 2^1 O(\frac{n}{2}) + \dots + 2^{i-1} O(\frac{n}{2^{i-1}}) = O(n \log n)$ for $i = \log_2 n$, achieving *linear* space with *log-linear* time.

In the case that d is not a small constant (i.e. where one does not assume a low-rank factorization of cost matrix $C = AB^T$), the time and space complexity becomes quadratic in n , like Sinkhorn. We use the sample-linear algorithm of (Indyk et al., 2019) to compute a factorization of the distance matrix, which applies to any distance $c(\cdot, \cdot)$ satisfying metric properties such as the triangle inequality (see Appendix E.1). For the squared Euclidean cost, as noted in (Scetbon et al., 2021), one may efficiently compute a $(d + 2)$ dimensional factorization where d is the data dimension, so under this cost one may achieve log-linear scaling without any approximation error on the distance. We observe this scaling empirically, as reported in Fig. S2.

4. Experiments

We benchmark Hierarchical Refinement (HiRef) against the full-rank OT methods Sinkhorn (Cuturi, 2013), the de

facto standard for computing OT alignments, and ProgOT (Kassraie et al., 2024), as well as the low-rank OT methods LOT (Scetbon et al., 2021) and FRLC (Halmos et al., 2024). We do not benchmark against the multiscale method MOP (Gerber & Maggioni, 2017), as computing a multiscale alignment depends on multiscale partitions of each dataset given as input, which are akin to a family of dyadic cubes across scales and lead to a transport cost that depends on the choice of this partition.

4.1. Evaluation on Synthetic Datasets.

We first evaluate the performance of Hierarchical Refinement against optimal transport methods returning primal couplings, namely Sinkhorn (Cuturi, 2013) (as implemented in `ott-jax`) and ProgOT (Kassraie et al., 2024). We evaluate the methods with respect to the Wasserstein-1 and Wasserstein-2 distance on an alignment of 1024 pairs of samples on the Checkerboard (Makkuva et al., 2020), MAF-Moons and Rings (Buzun et al., 2024), and Half-Moon and S-Curve (Buzun et al., 2024) synthetic datasets (Fig. 3, Table S6).

All methods are similarly effective at minimizing the primal OT cost $\langle C, P \rangle_F$, with small absolute difference in cost between the final couplings. Hierarchical Refinement achieves slightly lower primal cost on 4 out of the 6 evaluations. Notably, there is a massive difference in the number of non-zero entries (defined as entries $P_{ij} > 10^{-8}$) in the couplings output by HiRef, Sinkhorn, and ProgOT (Table S3).

Specifically, across the experiments HiRef outputs a bijection with exactly 1024 non-zero elements in the coupling matrix, equal to the number of aligned samples. In contrast, Sinkhorn and ProgOT output couplings with 624,733 to 678,720 and 271,087 to 337,258 non-zero entries, respectively. Moreover, the entropy of the HiRef coupling matrix is approximately half that of both Sinkhorn and ProgOT.

We also compare the cost of couplings computed by Hierarchical Refinement to low-rank couplings (Scetbon et al., 2021; Halmos et al., 2024) of varying rank. We observe that as the latent rank $r \rightarrow n$, the OT cost $\langle C, P_r \rangle_F$ asymptotically approaches the cost achieved by Hierarchical Refinement (Figure S3). In the limit $\lim_{r \rightarrow n} \langle C, P_r \rangle_F$ low-rank OT recovers Sinkhorn (Scetbon & Cuturi, 2022) and approaches quadratic memory complexity, while HiRef remains linear in space.

We evaluate the scalability of Hierarchical Refinement relative to other full-rank solvers on varying numbers of samples from the Half Moon & S-Curve (Buzun et al., 2024) synthetic dataset. We vary the rank from $2^5 = 32$ (64 points aligned) up to $2^{20} = 1,048,576$ points (2,097,152 points aligned) in \mathbb{R}^2 , the latter dataset of a size that is beyond

Table 1. Cost Values $\langle C, P \rangle_F$ Across Early Embryonic Stages

Method	E9.5-10.5	E10.5-11.5	E11.5-12.5
HiRef	21.81	14.81	16.14
Sinkhorn	21.91	14.89	N/A
ProgOT	22.56	15.35	N/A
FRLC ($r = 40$)	23.14	16.09	17.74
LOT ($r = 40$)	26.06	19.06	21.64

 Table 2. Cost Values $\langle C, P \rangle_F$ Across Later Embryonic Stages

Method	E12-13.5	E13-14.5	E14-15.5	E15-16.5
HiRef	14.57	13.78	14.29	12.79
Sinkhorn	N/A	N/A	N/A	N/A
ProgOT	N/A	N/A	N/A	N/A
FRLC	15.47	14.64	15.51	14.00
LOT	-	-	-	-

the capabilities of current optimal transport solvers. We observe that Sinkhorn (Cuturi, 2013) and ProgOT – methods which produce dense mappings – require a coupling matrix with $O(n^2)$ non-zero entries and thus run only up to 16,384 points. HiRef yields solutions with comparable primal cost to ProgOT and Sinkhorn on the sample sizes where all methods run.

In contrast, Hierarchical Refinement scales to over a million points, two orders of magnitude greater, while maintaining OT cost competitive with the dual revised simplex solver (Huangfu & Hall, 2017), which runs only up to 512 points (Table S4). This solver outputs an *optimal* plan, unlike ProgOT, Sinkhorn, and HiRef which rely on entropic regularization. HiRef scales linearly with the problem instance – albeit with a large constant – (Fig. S2a) in contrast to the quadratic scaling in time complexity of Sinkhorn (Fig. S2b).

4.2. Large-scale Matching Problems and Transcriptomics

Recently, optimal transport has been applied to single-cell and spatial transcriptomics datasets to compute couplings between cells taken from different timepoints from developmental processes or perturbations (Schiebinger et al., 2019; Lavenant et al., 2021; Bunne et al., 2022; Huizing et al., 2024; Halmos et al., 2025b; Klein et al., 2025). However, the size of current datasets (Chen et al., 2022) ($> 100,000$ cells) has exceeded the capacity of existing full-rank solvers, requiring low-rank approximations of the plan (Scetbon et al., 2023; Klein et al., 2025; Halmos et al., 2025a) to produce alignments.

We evaluate whether the full-rank solver of Hierarchical Refinement exhibits competitive alignments for such datasets. Specifically, we analyze the mouse organogenesis spatiotemporal transcriptomic atlas (MOSTA) datasets, which include spatial transcriptomics data from mouse embryos at suc-

cessive 1-day time-intervals with increasing number n of cells at each stage: E9.5 ($n = 5, 913$), E10.5 ($n = 18, 408$), E11.5 ($n = 30, 124$), E12.5 ($n = 51, 365$), E13.5 ($n = 77, 369$), E14.5 ($n = 102, 519$), E15.5 ($n = 113, 350$), and E16.5 ($n = 121, 767$). For the cost we use the Euclidean distance $C_{ij} = \|\mathbf{x}_i - \mathbf{y}_j\|_2$ in 60-dimensional PCA space of expression vectors, so $\mathbf{x}_i, \mathbf{y}_j \in \mathbb{R}^{60}$.

Sinkhorn and ProgOT are unable to produce alignments for the stages beyond E10.5 ($n = 18, 408$ cells), whereas HiRef and low-rank solvers are able to continue scaling to $> 10^5$ (Table 1). We observe that the Kantorovich cost of HiRef is consistently lower than all other methods for all timepoints (Table 1).

In particular, HiRef achieves a substantially lower cost than the low-rank solvers FRLC and LOT for rank $r = 40$, even though HiRef relies on low-rank optimal transport (FRLC) as a sub-routine. This underscores the empirical trend observed in Fig. S3, where the cost of HiRef is lower than the cost of its low-rank subroutines. While LOT (Scetbon et al., 2021) provides a robust, scalable low-rank procedure for the Wasserstein-2 distance, the LOT solver with point cloud input on Wasserstein-1 cost only runs for the first pair (E9.5:E10.5). For subsequent pairs we input the cost C directly, resulting in the LOT solver running up to the third pair (E11.5:E12.5).

4.3. MERFISH Brain Atlas Alignment

We ran HiRef on two slices of MERFISH Mouse Brain Receptor Map data from Vizgen to test whether HiRef can produce biologically valid alignments using the *only* spatial densities of each tissue. These spatial transcriptomics data consist of spatial and gene expression measurements at individual spots in three full coronal slices across three biological replicates. Our “source” dataset $(\mathbf{X}^1, \mathbf{S}^1)$ is replicate 3 of slice 2, while our “target” dataset $(\mathbf{X}^2, \mathbf{S}^2)$ is replicate 2 of slice 2, following the expression transfer task described (Clifton et al., 2023) between these two slices. Each dataset has roughly 84k spots, where memory constraints prohibit instantiation a full-rank alignment as a matrix. Thus, solvers such as Sinkhorn (Cuturi, 2013) and ProgOT (Kassraie et al., 2024) are unable to run on the dataset.

We use only spatial information when building a map between the two slices, using spatial cost matrix $C_{ij} := \|\mathbf{s}_i^1 - \mathbf{s}_j^2\|_2$ as input to HiRef, after registering spatial coordinates $\mathbf{S}^1 = \{\mathbf{s}_i^1\}_{i=1}^n$ and $\mathbf{S}^2 = \{\mathbf{s}_i^2\}_{i=1}^n$ with an affine transformation. We gauged the quality of the HiRef alignment (Fig. 4a), using gene expression abundances of five “spatially-varying” genes. Specifically, we observe that expression vector \mathbf{v}^1 of gene *Slc17a7* in the source slice (Fig. 4b) when transferred to target slice through the bijective mapping output by HiRef, denoted as $\hat{\mathbf{v}}$ (Fig. 4c), closely match the observed expression vector \mathbf{v}^2 of *Slc17a7* in the

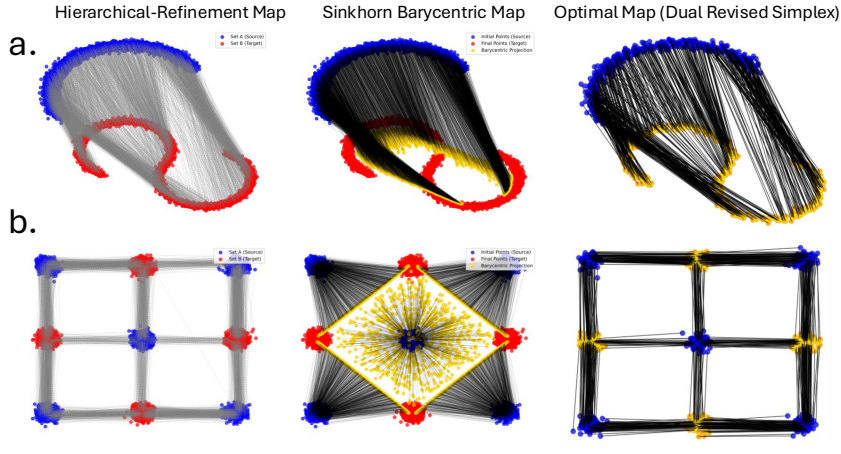


Figure 3. Comparison of the Hierarchical Refinement Mapping, the Sinkhorn Barycentric Map, and an optimal map computing using dual revised simplex for the **a.** Half-moon and S-curve dataset (Buzun et al., 2024) of 4096 points (512 points for dual revised simplex) and **b.** Checkerboard dataset (Makkuva et al., 2020).

Table 3. Cost Values $\langle C, P \rangle_F$ for ImageNet (Deng et al., 2009; Russakovsky et al., 2015) Alignment Task.

Method	HiRef	Sinkhorn	ProgOT	FRLC	LOT
OT Cost	18.974	N/A	N/A	24.119	N/A

target slice (Fig. 4d) with cosine similarity equal to 0.8098. For the genes (*Grm4*, *Olig1*, *Gad1*, *Peg10*), the corresponding cosine similarities between the transferred and observed expression vectors are 0.7959, 0.7526, 0.4932, and 0.6015.

For comparison, we also ran the low-rank methods FRLC (Halmos et al., 2024) and LOT (Scetbon et al., 2021). For the gene *Slc17a7*, FRLC’s cosine similarity was .2098, while LOT’s cosine similarity was 0.3241. For the other four genes (*Grm4*, *Olig1*, *Gad1*, *Peg10*), FRLC’s scores were (0.2072, 0.1756, 0.0959, 0.0692), and LOT’s scores were (0.2279, 0.3029, 0.1653, 0.0719). Across all five genes HiRef’s scores were at least twice those of FRLC or LOT (Table S7) with gene abundances shown in Fig. S1. Further experimental details are in Section D.3.

4.4. ImageNet Alignment

We demonstrate the scalability of Hierarchical Refinement to massive and high-dimensional datasets by performing an alignment of 2048-dimensional embeddings of 1.281 million images from the ImageNet ILSVRC dataset (Deng et al., 2009; Russakovsky et al., 2015). Specifically, we generate a 2048-dimensional embedding of each image using the ResNet50 architecture (He et al., 2016) and take a random 50:50 split of the embedded images to generate datasets X and Y. We align X and Y using HiRef and FRLC, as

ProgOT, Sinkhorn, and LOT were not able to run on the data. HiRef yielded a primal OT cost of 18.974, while FRLC (Halmos et al., 2024) solution had a primal OT cost of 24.119 for rank $r = 40$ (Table 3).

5. Discussion

Hierarchical Refinement computes optimal bijective couplings between large-scale datasets in linear space, but has several limitations. First, we currently assume that the datasets X and Y have the same number of samples. In many machine learning applications, this is not a substantial concern, as one generally seeks to pair an equal number of source points x to target points y . Second, while Hierarchical Refinement scales linearly in space and time, it still involves a large constant dependent on the low-rank OT sub-procedure used – this implies the need to accelerate and stabilize low-rank OT solvers further (Scetbon & Cuturi, 2022; Halmos et al., 2024). Third, while Hierarchical Refinement guarantees an optimal solution given an optimal black-box low-rank solver (Proposition 3.1), the low-rank solvers (Scetbon et al., 2022; Halmos et al., 2024) used in practice are not necessarily optimal, owing to the non-convexity of low-rank problems. Finally, the rank-schedule used in Hierarchical Refinement requires a non-trivial factorization of n , and thus requires datasets that do not have a prime number of samples. Of course, this limitation can be bypassed through light sub-sampling of one or both datasets, provided they are of comparable size.

Hierarchical Refinement may be useful in neural OT approaches which learn a continuous Monge map between the densities of two datasets. For example, (Seguy et al., 2018)

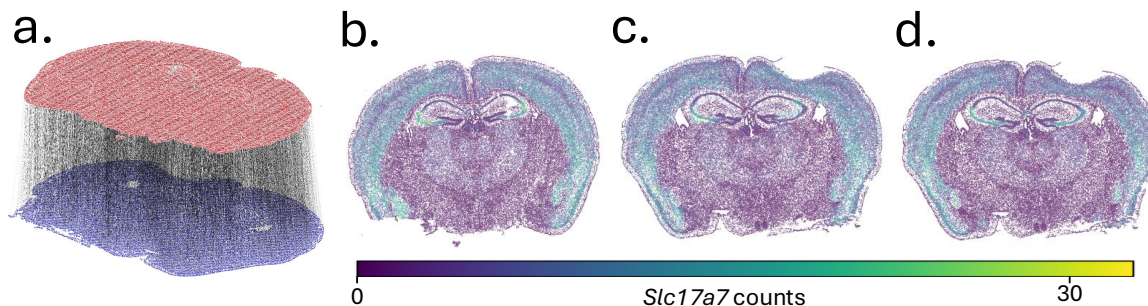


Figure 4. **a.** Hierarchical Refinement alignment on MERFISH mouse brain data, using only spatial coordinates. **b.** Abundance \mathbf{v}^1 of gene *Slc17a7* in the source slice. **c.** Predicted *Slc17a7* abundance $\hat{\mathbf{v}}$ from the source slice to the target slice, through the HiRef transport plan. **d.** Abundance \mathbf{v}^2 of the same gene in the target slice. Transferred abundances $\hat{\mathbf{v}}$ have cosine similarity 0.8098 with true abundances \mathbf{v}^2 in the target.

minimize a loss $\min_{\theta} \frac{1}{2} \mathbb{E}_{\mu} \|T_{\theta}(\mathbf{x}_i) - T(\mathbf{x}_i)\|_2^2$ between a neural network T_{θ} with parameters θ and a Monge map T over samples $\mathbf{x}_i \sim \mu$ (Remark B.7). Hierarchical Refinement can generate datasets of Monge map pairs $(\mathbf{x}_i, T(\mathbf{x}_i))$ from unpaired samples $(\mathbf{x}_i)_{i=1}^n$ and $(\mathbf{y}_i)_{i=1}^n$. This suggests one may directly train a neural network T_{θ} to match these pairs, without the bias of mini-batching.

6. Conclusion

We introduce Hierarchical Refinement (HiRef), an algorithm to solve optimal transport problems with linear space complexity in the number of datapoints, making sparse, full-rank optimal transport feasible for large-scale datasets. Our algorithm leverages that low-rank optimal transport co-clusters points with their image under the Monge map, progressively refining bijections between partitions of each dataset across a hierarchy of scales, down to a bijective alignment between the datasets at the finest scale. We demonstrate that Hierarchical Refinement plans achieve comparable or better primal cost than plans obtained through full-rank entropic solvers, and that the algorithm scales to datasets with over a million points. We argue that Hierarchical Refinement’s ability to compute alignments between massive datasets will open the door to applications that were previously infeasible for optimal transport.

Acknowledgements

We thank Henri Schmidt for many helpful conversations. This research was supported by NIH/NCI grant U24CA248453 to B.J.R. J.G. is supported by the Schmidt DataX Fund at Princeton University made possible through a major gift from the Schmidt Futures Foundation.

Code Availability

Our implementation of Hierarchical Refinement is available at <https://github.com/raphael-group/HiRef>.

References

- Aurenhammer, F., Hoffmann, F., and Aronov, B. Minkowski-type theorems and least-squares clustering. *Algorithmica*, 20:61–76, 1998.
- Brenier, Y. Polar factorization and monotone rearrangement of vector-valued functions. *Communications on pure and applied mathematics*, 44(4):375–417, 1991.
- Bunne, C., Meng-Papaxanthos, L., Krause, A., and Cuturi, M. Proximal Optimal Transport Modeling of Population Dynamics. In *International Conference on Artificial Intelligence and Statistics (AISTATS)*, volume 25, 2022.
- Bunne, C., Stark, S. G., Gut, G., del Castillo, J. S., Levesque, M., Lehmann, K.-V., Pelkmans, L., Krause, A., and Ratsch, G. Learning single-cell perturbation responses using neural optimal transport. *Nature Methods*, 20(11):1759–1768, September 2023. ISSN 1548-7105. doi: 10.1038/s41592-023-01969-x. URL <http://dx.doi.org/10.1038/s41592-023-01969-x>.
- Buzun, N., Bobrin, M., and Dylov, D. V. Expectile regularization for fast and accurate training of neural optimal transport. In *The Thirty-eighth Annual Conference on Neural Information Processing Systems*, 2024. URL <https://openreview.net/forum?id=4DA5vaPHFb>.
- Chen, A., Liao, S., Cheng, M., Ma, K., Wu, L., Lai, Y., Qiu, X., Yang, J., Xu, J., Hao, S., et al. Spatiotemporal transcriptomic atlas of mouse organogenesis using DNA nanoball-patterned arrays. *Cell*, 185(10):1777–1792, 2022.

- Chen, J., Chen, L., Liu, Y. P., Peng, R., and Ramaswami, A. *Exponential Convergence of Sinkhorn Under Regularization Scheduling*, pp. 180–188. Society for Industrial and Applied Mathematics, January 2023. ISBN 9781611977714. doi: 10.1137/1.9781611977714.16. URL <http://dx.doi.org/10.1137/1.9781611977714.16>.
- Chen, X. and Price, E. Condition number-free query and active learning of linear families. 2017.
- Clifton, K., Anant, M., Aihara, G., Atta, L., Aimiwu, O. K., Kebschull, J. M., Miller, M. I., Tward, D., and Fan, J. Stalign: Alignment of spatial transcriptomics data using diffeomorphic metric mapping. *Nature communications*, 14(1):8123, 2023.
- Cohen, J. E. and Rothblum, U. G. Nonnegative Ranks, Decompositions, and Factorizations of Nonnegative Matrices. *Linear Algebra and its Applications*, 190:149–168, 1993.
- Courty, N., Flamary, R., and Tuia, D. Domain adaptation with regularized optimal transport. In *Machine Learning and Knowledge Discovery in Databases: European Conference, ECML PKDD 2014, Nancy, France, September 15-19, 2014. Proceedings, Part I 14*, pp. 274–289. Springer, 2014.
- Cuturi, M. Sinkhorn distances: Lightspeed computation of optimal transport. *Advances in Neural Information Processing Systems*, pp. 2292–2300, 2013.
- De Bortoli, V., Thornton, J., Heng, J., and Doucet, A. Diffusion schrödinger bridge with applications to score-based generative modeling. *arXiv preprint arXiv:2106.01357*, 2021.
- De Bortoli, V., Korshunova, I., Mnih, A., and Doucet, A. Schrodinger bridge flow for unpaired data translation. In *The Thirty-eighth Annual Conference on Neural Information Processing Systems*, 2024. URL <https://openreview.net/forum?id=1F32iCJFfa>.
- De Loera, J. A. and Kim, E. D. Combinatorics and geometry of transportation polytopes: An update. *arXiv: Combinatorics*, 2013. URL <https://api.semanticscholar.org/CorpusID:119645112>.
- Deng, J., Socher, R., Fei-Fei, L., Dong, W., Li, K., and Li, L.-J. Imagenet: A large-scale hierarchical image database. In *2009 IEEE Conference on Computer Vision and Pattern Recognition(CVPR)*, volume 00, pp. 248–255, 06 2009. doi: 10.1109/CVPR.2009.5206848. URL <https://ieeexplore.ieee.org/abstract/document/5206848/>.
- Fan, J., Liu, S., Ma, S., Zhou, H.-M., and Chen, Y. Neural monge map estimation and its applications. *Transactions on Machine Learning Research*, 2023. ISSN 2835-8856. URL <https://openreview.net/forum?id=2mZSlQscj3>. Featured Certification.
- Fatras, K., Séjourné, T., Courty, N., and Flamary, R. Unbalanced minibatch optimal transport; applications to domain adaptation. In *Proceedings of the 38th International Conference on Machine Learning*, 2021.
- Finlay, C., Jacobsen, J.-H., Nurbekyan, L., and Oberman, A. M. How to train your neural ode: the world of jacobian and kinetic regularization, 2020. URL <https://arxiv.org/abs/2002.02798>.
- Forrow, A., Hütter, J.-C., Nitzan, M., Rigollet, P., Schiebinger, G., and Weed, J. Statistical Optimal Transport via Factored Couplings. In Chaudhuri, K. and Sugiyama, M. (eds.), *Proceedings of the Twenty-Second International Conference on Artificial Intelligence and Statistics*, volume 89 of *Proceedings of Machine Learning Research*, pp. 2454–2465. PMLR, 16–18 Apr 2019. URL <https://proceedings.mlr.press/v89/forrow19a.html>.
- Frieze, A., Kannan, R., and Vempala, S. Fast Monte-Carlo Algorithms for Finding Low-rank Approximations. *J. ACM*, 51(6):1025–1041, nov 2004. ISSN 0004-5411. doi: 10.1145/1039488.1039494. URL <https://doi.org/10.1145/1039488.1039494>.
- Genevay, A., Peyre, G., and Cuturi, M. Learning generative models with sinkhorn divergences. In Storkey, A. and Perez-Cruz, F. (eds.), *Proceedings of the Twenty-First International Conference on Artificial Intelligence and Statistics*, volume 84 of *Proceedings of Machine Learning Research*, pp. 1608–1617. PMLR, 09–11 Apr 2018. URL <https://proceedings.mlr.press/v84/genevay18a.html>.
- Gerber, S. and Maggioni, M. Multiscale strategies for computing optimal transport. *Journal of Machine Learning Research*, 18(72):1–32, 2017.
- Geshkovski, B., Letrouit, C., Polyanskiy, Y., and Rigollet, P. A mathematical perspective on Transformers. *arXiv preprint arXiv:2312.10794*, 2023.
- Glimm, T. and Henscheid, N. Iterative scheme for solving optimal transportation problems arising in reflector design. *International Scholarly Research Notices*, 2013(1): 635263, 2013.

- Halmos, P., Liu, X., Gold, J., and Raphael, B. Low-Rank Optimal Transport through Factor Relaxation with Latent Coupling. In *The Thirty-eighth Annual Conference on Neural Information Processing Systems*, 2024. URL <https://openreview.net/forum?id=hGgkdFF2hR>.
- Halmos, P., Gold, J., Liu, X., and Raphael, B. J. Learning latent trajectories in developmental time series with hidden-markov optimal transport. February 2025a. doi: 10.1101/2025.02.14.638351. URL <http://dx.doi.org/10.1101/2025.02.14.638351>.
- Halmos, P., Liu, X., Gold, J., Chen, F., Ding, L., and Raphael, B. J. DeST-OT: Alignment of spatiotemporal transcriptomics data. *Cell Systems*, January 2025b. ISSN 2405-4712. doi: 10.1016/j.cels.2024.12.001. URL <http://dx.doi.org/10.1016/j.cels.2024.12.001>.
- He, K., Zhang, X., Ren, S., and Sun, J. Deep residual learning for image recognition. In *Proceedings of the IEEE conference on computer vision and pattern recognition*, pp. 770–778, 2016.
- Huangfu, Q. and Hall, J. A. J. Parallelizing the dual revised simplex method. *Mathematical Programming Computation*, 10(1):119–142, December 2017. ISSN 1867-2957. doi: 10.1007/s12532-017-0130-5. URL <http://dx.doi.org/10.1007/s12532-017-0130-5>.
- Huizing, G.-J., Peyré, G., and Cantini, L. Learning cell fate landscapes from spatial transcriptomics using fused gromov-wasserstein. July 2024. doi: 10.1101/2024.07.26.605241. URL <http://dx.doi.org/10.1101/2024.07.26.605241>.
- Indyk, P., Vakilian, A., Wagner, T., and Woodruff, D. P. Sample-optimal low-rank approximation of distance matrices. In Beygelzimer, A. and Hsu, D. (eds.), *Proceedings of the Thirty-Second Conference on Learning Theory*, volume 99 of *Proceedings of Machine Learning Research*, pp. 1723–1751. PMLR, 25–28 Jun 2019. URL <https://proceedings.mlr.press/v99/indyk19a.html>.
- Kantorovich, L. On the Translocation of Masses: Doklady akademii nauk ussr. 1942.
- Kassraie, P., Pooladian, A.-A., Klein, M., Thornton, J., Niles-Weed, J., and Cuturi, M. Progressive entropic optimal transport solvers. *arXiv preprint arXiv:2406.05061*, 2024.
- Klein, D., Uscidda, T., Theis, F. J., and marco cuturi. Generative entropic neural optimal transport to map within and across space, 2024. URL <https://openreview.net/forum?id=gBLEHzKOFF>.
- Klein, D., Palla, G., Lange, M., Klein, M., Piran, Z., Gander, M., Meng-Papaxanthos, L., Sterr, M., Saber, L., Jing, C., Bastidas-Ponce, A., Cota, P., Tarquis-Medina, M., Parikh, S., Gold, I., Lickert, H., Bakhti, M., Nitzan, M., Cuturi, M., and Theis, F. J. Mapping cells through time and space with moscot. *Nature*, January 2025. ISSN 1476-4687. doi: 10.1038/s41586-024-08453-2. URL <http://dx.doi.org/10.1038/s41586-024-08453-2>.
- Kornilov, N. M., Mokrov, P., Gasnikov, A., and Korotin, A. Optimal flow matching: Learning straight trajectories in just one step. In *The Thirty-eighth Annual Conference on Neural Information Processing Systems*, 2024. URL <https://openreview.net/forum?id=kqmucDKVcU>.
- Korotin, A., Li, L., Genevay, A., Solomon, J. M., Filippov, A., and Burnaev, E. Do neural optimal transport solvers work? a continuous wasserstein-2 benchmark. In *NeurIPS*, pp. 14593–14605, 2021. URL <http://dblp.uni-trier.de/db/conf/nips/neurips2021.html#KorotinLGSFB21>.
- Korotin, A., Selikhanovych, D., and Burnaev, E. Neural optimal transport. In *The Eleventh International Conference on Learning Representations*, 2023. URL <https://openreview.net/forum?id=d8CBRLWNkqH>.
- Kuhn, H. W. The Hungarian Method for the Assignment Problem. *Naval Research Logistics Quarterly*, 2(1–2): 83–97, March 1955. doi: 10.1002/nav.3800020109.
- Lavenant, H., Zhang, S., Kim, Y.-H., and Schiebinger, G. Towards a mathematical theory of trajectory inference. *arXiv preprint arXiv:2102.09204*, 2021.
- Li, X., Chen, J., Chai, Y., and Xiong, H. GiLOT: Interpreting generative language models via optimal transport. In *Forty-first International Conference on Machine Learning*, 2024. URL <https://openreview.net/forum?id=qKL25sGjxL>.
- Lin, C.-H., Azabou, M., and Dyer, E. L. Making transport more robust and interpretable by moving data through a small number of anchor points. *Proceedings of machine learning research*, 139:6631, 2021.
- Luo, J., Yang, D., and Wei, K. Improved complexity analysis of the sinkhorn and greenhorn algorithms for optimal transport. *arXiv preprint arXiv:2305.14939*, 2023.
- Makkuva, A., Taghvaei, A., Oh, S., and Lee, J. Optimal transport mapping via input convex neural networks. In III, H. D. and Singh, A. (eds.), *Proceedings of the 37th International Conference on Machine Learning*, volume 119 of *Proceedings of Machine Learning Research*, 2023.

- Learning Research*, pp. 6672–6681. PMLR, 13–18 Jul 2020. URL <https://proceedings.mlr.press/v119/makkuva20a.html>.
- Melnyk, I., Mroueh, Y., Belgodere, B., Rigotti, M., Nit-sure, A., Yurochkin, M., Greenewald, K., Navratil, J., and Ross, J. Distributional preference alignment of LLMs via optimal transport. In *The Thirty-eighth Annual Conference on Neural Information Processing Systems*, 2024. URL <https://openreview.net/forum?id=2LctgfN6Ty>.
- Mérigot, Q. A multiscale approach to optimal transport. In *Computer graphics forum*, volume 30, pp. 1583–1592. Wiley Online Library, 2011.
- Monge, G. Mémoire sur la théorie des déblais et des remblais. *Mem. Math. Phys. Acad. Royale Sci.*, pp. 666–704, 1781.
- Oberman, A. M. and Ruan, Y. An efficient linear programming method for optimal transportation. *arXiv preprint arXiv:1509.03668*, 2015.
- Orlin, J. B. A polynomial time primal network simplex algorithm for minimum cost flows. *Mathematical Programming*, 78(2):109–129, Aug 1997. ISSN 1436-4646. doi: 10.1007/BF02614365. URL <https://link.springer.com/content/pdf/10.1007/BF02614365.pdf>.
- Peyré, G., Cuturi, M., et al. Computational optimal transport: With applications to data science. *Foundations and Trends® in Machine Learning*, 11(5-6):355–607, 2019.
- Ramesh, A., Pavlov, M., Goh, G., Gray, S., Voss, C., Radford, A., Chen, M., and Sutskever, I. Zero-shot text-to-image generation. In *ICML*, volume 139, 2021. URL <http://dblp.uni-trier.de/db/conf/icml/icml2021.html#RameshPGGVRCS21>.
- Russakovsky, O., Deng, J., Su, H., Krause, J., Satheesh, S., Ma, S., Huang, Z., Karpathy, A., Khosla, A., Bernstein, M., Berg, A. C., and Fei-Fei, L. ImageNet Large Scale Visual Recognition Challenge. *International Journal of Computer Vision (IJCV)*, 115(3):211–252, 2015. doi: 10.1007/s11263-015-0816-y.
- Sander, M. E., Ablin, P., Blondel, M., and Peyré, G. Sinkformers: Transformers with Doubly Stochastic Attention. In Camps-Valls, G., Ruiz, F. J. R., and Valera, I. (eds.), *Proceedings of The 25th International Conference on Artificial Intelligence and Statistics*, volume 151 of *Proceedings of Machine Learning Research*, pp. 3515–3530. PMLR, 28–30 Mar 2022. URL <https://proceedings.mlr.press/v151/sander22a.html>.
- Scetbon, M. and Cuturi, M. Low-rank Optimal Transport: Approximation, Statistics and Debiasing. In Oh, A. H., Agarwal, A., Belgrave, D., and Cho, K. (eds.), *Advances in Neural Information Processing Systems*, 2022. URL <https://openreview.net/forum?id=4btNeXKFAQ>.
- Scetbon, M., Cuturi, M., and Peyré, G. Low-Rank Sinkhorn Factorization. In *International Conference on Machine Learning*, 2021. URL <https://api.semanticscholar.org/CorpusID:232147563>.
- Scetbon, M., Peyré, G., and Cuturi, M. Linear-time Gromov Wasserstein Distances using Low Rank Couplings and Costs. In *International Conference on Machine Learning*, pp. 19347–19365. PMLR, 2022.
- Scetbon, M., Klein, M., Palla, G., and Cuturi, M. Unbalanced Low-rank Optimal Transport Solvers, 2023.
- Schiebinger, G., Shu, J., Tabaka, M., Cleary, B., Subramanian, V., Solomon, A., Gould, J., Liu, S., Lin, S., Berube, P., et al. Optimal-Transport Analysis of Single-Cell Gene Expression Identifies Developmental Trajectories in Reprogramming. *Cell*, 176(4):928–943, 2019.
- Schmitzer, B. A sparse multiscale algorithm for dense optimal transport. *Journal of Mathematical Imaging and Vision*, 56:238–259, 2016.
- Seguy, V., Damodaran, B. B., Flamary, R., Courty, N., Rolet, A., and Blondel, M. Large-scale optimal transport and mapping estimation. In *Proceedings of the International Conference in Learning Representations*, 2018.
- Sinkhorn, R. A relationship between arbitrary positive matrices and stochastic matrices. *Canadian Journal of Mathematics*, 18:303–306, 1966.
- Solomon, J., De Goes, F., Peyré, G., Cuturi, M., Butscher, A., Nguyen, A., Du, T., and Guibas, L. Convolutional Wasserstein Distances: Efficient Optimal Transportation on Geometric Domains. *ACM Transactions on Graphics (ToG)*, 34(4):1–11, 2015.
- Sommerfeld, M., Schrieber, J., Zemel, Y., and Munk, A. Optimal transport: Fast probabilistic approximation with exact solvers. *Journal of Machine Learning Research*, 20(105):1–23, 2019. URL <http://jmlr.org/papers/v20/18-079.html>.
- Ståhl, P. L., Salmén, F., Vickovic, S., Lundmark, A., Navarro, J. F., Magnusson, J., Giacomello, S., Asp, M., Westholm, J. O., Huss, M., et al. Visualization and analysis of gene expression in tissue sections by spatial transcriptomics. *Science*, 353(6294):78–82, 2016.

- Tarjan, R. E. Dynamic trees as search trees via Euler tours, applied to the network simplex algorithm. *Mathematical Programming*, 78(2):169–177, Aug 1997. ISSN 1436-4646. doi: 10.1007/BF02614369. URL <https://link.springer.com/content/pdf/10.1007/BF02614369.pdf>.
- Tay, Y., Bahri, D., Yang, L., Metzler, D., and Juan, D.-C. Sparse Sinkhorn Attention. In III, H. D. and Singh, A. (eds.), *Proceedings of the 37th International Conference on Machine Learning*, volume 119 of *Proceedings of Machine Learning Research*, pp. 9438–9447. PMLR, 13–18 Jul 2020. URL <https://proceedings.mlr.press/v119/tay20a.html>.
- Thorpe, M. Introduction to optimal transport. 2017. URL <https://api.semanticscholar.org/CorpusID:131768046>.
- Tong, A., Malkin, N., Huguet, G., Zhang, Y., Rector-Brooks, J., Fatras, K., Wolf, G., and Bengio, Y. Improving and generalizing flow-based generative models with mini-batch optimal transport. In *ICML Workshop on New Frontiers in Learning, Control, and Dynamical Systems*, 2023.
- Tong, A., FATRAS, K., Malkin, N., Huguet, G., Zhang, Y., Rector-Brooks, J., Wolf, G., and Bengio, Y. Improving and generalizing flow-based generative models with mini-batch optimal transport. *Transactions on Machine Learning Research*, 2024. ISSN 2835-8856. URL <https://openreview.net/forum?id=CD9Snc73AW>. Expert Certification.
- Wolf, F. A., Angerer, P., and Theis, F. J. SCANPY: large-scale single-cell gene expression data analysis. *Genome biology*, 19:1–5, 2018.
- Yang, K. D., Damodaran, K., Venkatachalapathy, S., Soylemezoglu, A. C., Shivashankar, G., and Uhler, C. Predicting cell lineages using autoencoders and optimal transport. *PLoS computational biology*, 16(4):e1007828, 2020.
- Zeira, R., Land, M., Strzalkowski, A., and Raphael, B. J. Alignment and integration of spatial transcriptomics data. *Nature Methods*, 19(5):567–575, 2022.

A. Algorithm for Hierarchical-Refinement

Algorithm 2 Hierarchical Refinement for Full-Rank OT

Require: Datasets $X = \{\mathbf{x}_i\}_{i=1}^n$, $Y = \{\mathbf{y}_i\}_{i=1}^n$; **Low-rank OT solver** $\text{LROT}(\cdot)$; **Rank schedule** $(r_1, r_2, \dots, r_\kappa)$;
Base rank $r_{\text{base}} = \frac{n}{\prod_{t=1}^{\kappa} r_t}$ (e.g. 1).
Initialize:
 1: $t \leftarrow 0, \Gamma_0 \leftarrow \{(X, Y)\}$
 2: **while** $\exists (X^{(t)}, Y^{(t)}) \in \Gamma_t$ **with**
 3: $\min\{|X^{(t)}|, |Y^{(t)}|\} > r_{\text{base}}$ **do**
 4: $\Gamma_{t+1} \leftarrow \emptyset$
 5: **for** $(X_q^{(t)}, Y_q^{(t)}) \in \Gamma_t$ **do**
 6: **if** $\min\{|X_q^{(t)}|, |Y_q^{(t)}|\} \leq r_{\text{base}}$ **then**
 7: $\Gamma_{t+1} \leftarrow \Gamma_{t+1} \cup \{(X_q^{(t)}, Y_q^{(t)})\}$
 8: **else**
 9: $\mu_{X_q^{(t)}} = \frac{1}{|X_q^{(t)}|} \sum_{\mathbf{x} \in X_q^{(t)}} \delta_{\mathbf{x}}$
 10: $\mu_{Y_q^{(t)}} = \frac{1}{|Y_q^{(t)}|} \sum_{\mathbf{y} \in Y_q^{(t)}} \delta_{\mathbf{y}}$.
 11: $\mathbf{u} \leftarrow \text{UniformInit}(r_{t+1})$ $\triangleright u_i = 1/r_{t+1}$
 12: $(\mathbf{Q}, \mathbf{R}) \leftarrow \text{LROT}(\mu_{X_q^{(t)}}, \mu_{Y_q^{(t)}}, r_{t+1}, \mathbf{u})$
 13: **for** $z = 1 \rightarrow r_{t+1}$ **do**
 14: $X_z^{(t+1)} \leftarrow \text{Select}(X^{(t)}, \mathbf{Q}, z)$
 15: $Y_z^{(t+1)} \leftarrow \text{Select}(Y^{(t)}, \mathbf{R}, z)$
 16: $\Gamma_{t+1} \leftarrow \Gamma_{t+1} \cup \{(X_z^{(t+1)}, Y_z^{(t+1)})\}$
 17: **end for**
 18: $\triangleright \text{Select}(S, \mathbf{M}, z) = \{s \in S \mid \arg \max_{z'} \mathbf{M}_{sz'} = z\}$
 19: **end if**
 20: **end for**
 21: $t \leftarrow t + 1$
 22: **end while**
 23: **Output:** $\Gamma_t = \{(\mathbf{x}_i, T(\mathbf{x}_i))\}$ \triangleright Set of refined pairs.

B. Proofs

Below, we suppose cost function $c : \mathbb{R}^d \times \mathbb{R}^d \rightarrow \mathbb{R}_+$ has the form $c(\mathbf{x}, \mathbf{y}) = h(\mathbf{x} - \mathbf{y})$ for some strictly convex function $h : \mathbb{R}^d \rightarrow \mathbb{R}_+$. We additionally assume that h is Lipschitz. For datasets $X, Y \subset \mathbb{R}^d$ with $|X| = |Y| = n$, with n assumed to be a power of 2, we form the cost matrix \mathbf{C} defined by

$$\mathbf{C}_{ij} := c(\mathbf{x}_i, \mathbf{y}_j). \quad (\text{S1})$$

The uniform weights on X and Y are denoted \mathbf{a}, \mathbf{b} respectively. In all cases below, we are concerned with the Kantorovich problem (3) for this cost matrix. We will first show that the optimal factors \mathbf{Q}, \mathbf{R} for the rank-2 Wasserstein problem given in (5) correspond to clusterings of each dataset. Let $\text{supp}_i(\mathbf{Q}) \subset [n]$ be the indices on which column i of \mathbf{Q} is supported, where $i = 1, 2$.

Lemma B.1. *Let $(\mathbf{Q}^*, \mathbf{R}^*)$ be optimal for the rank-2 Wasserstein problem (5) subject to the additional constraint that $\mathbf{a}, \mathbf{b}, \mathbf{g}$ are uniform and that n, m are even. Then, $(\text{supp}_1(\mathbf{Q}^*), \text{supp}_2(\mathbf{Q}^*))$ is a partition of $[n]$, and symmetrically, so is $(\text{supp}_1(\mathbf{R}^*), \text{supp}_2(\mathbf{R}^*))$.*

Proof. The cost is linear in (\mathbf{Q}, \mathbf{R}) respectively: the minimization in each variable given the other fixed can be expressed as

$$\arg \min_{\mathbf{Q} \in \Pi(\mathbf{a}, \mathbf{g})} \langle \mathbf{Q}, \mathbf{C} \mathbf{R} \text{diag}(1/\mathbf{g}) \rangle_F,$$

and

$$\arg \min_{\mathbf{R} \in \Pi(\mathbf{b}, \mathbf{g})} \langle \mathbf{R}, \mathbf{C}^T \mathbf{Q} \text{diag}(1/\mathbf{g}) \rangle_F.$$

Thus for any optimal \mathbf{Q}^* or \mathbf{R}^* fixed the minimization in the other variable is a linear optimal transport problem, where by Corollary 2.11 in (De Loera & Kim, 2013) it holds that since the constraint matrix is totally unimodular with marginals integral (on rescaling), the optima \mathbf{R}^* and \mathbf{Q}^* must be vertices on the transport polytopes $\Pi_{\mathbf{b},\mathbf{g}}$ and $\Pi_{\mathbf{a},\mathbf{g}}$ with integral entries (on rescaling, by $2n$ or $2m$). There are $\leq n + 1$ positive entries in any optimal rank $r = 2$ solution (De Loera & Kim, 2013; Peyré et al., 2019), so that n (resp. m) being even and the rescaled rows and columns summing to 2 and n implies that there are exactly n positive entries and thus that the vertices define partitions of $[n]$ and $[m]$. \square

Notably, in the case of an odd number of points n or m this likewise implies that one has a single row which has 2 entries $(1/2n \ 1/2n)$, with all other rows of the form $(0 \ 1/n)$ or $(1/n \ 0)$ defining a partition of the remaining even subset of size $(n - 1)$ or $(m - 1)$. In the general case of ranks $r \neq 2$ there are maximally $n + r + 1$ (Peyré et al., 2019) non-zero edges (so that the graph is acyclic), and for $n \gg r$ the optimal solution may remain close to a partition.

Using Lemma B.1, we show that optimal low-rank couplings $(\mathbf{Q}^*, \mathbf{R}^*, \mathbf{g}^*)$ co-cluster points $\mathbf{x} \in \mathbf{X}$ with their image under Monge map $T^*(\mathbf{x})$, when T^* exists. This co-clustering is in the sense of the clustering functions q^*, r^* (7) corresponding to each factor $\mathbf{Q}^*, \mathbf{R}^*$. We note that when μ and ν are discretely supported measures with supports of equal cardinality, a Monge map, $T^* : \mathbf{X} \rightarrow \mathbf{Y}$, is guaranteed to exist by Theorem 2.7 of (Thorpe, 2017).

Proposition B.2 (Proposition 3.1, optimal low-rank factors co-cluster Monge pairs). *Let $\mathbf{X}, \mathbf{Y} \subset \mathbb{R}^d$ with $|\mathbf{X}| = |\mathbf{Y}| = n = 2^k$, each equipped with uniform measures $\mathbf{a}, \mathbf{b} \in \Delta_n$, with all entries of cost matrix (S1) distinct. Suppose that $(\mathbf{Q}^*, \mathbf{R}^*)$ is optimal for the problem (5) with $r = 2$ and subject to the additional constraint that \mathbf{g} is uniform. Then for all $\mathbf{x} \in \mathbf{X}$, one has $q^*(\mathbf{x}) = r^* \circ T^*(\mathbf{x})$.*

Proof. Let $\mathbf{Q}^*, \mathbf{R}^*, T^*$ be as above, and write \mathbf{Q}, \mathbf{R} , and T instead for brevity. By Lemma B.1, \mathbf{Q} and \mathbf{R} correspond to the cluster assignments $q : \mathbf{X} \mapsto \{1, 2\}$, $r : \mathbf{Y} \mapsto \{1, 2\}$, where for $z = 1, 2$, one has:

$$\mathbf{Q}_{iz} = \begin{cases} \frac{1}{n} & \text{if } q(\mathbf{x}_i) = z \\ 0 & \text{otherwise} \end{cases}, \quad \mathbf{R}_{jz} = \begin{cases} \frac{1}{n} & \text{if } r(\mathbf{y}_j) = z \\ 0 & \text{otherwise} \end{cases}.$$

As these clusterings use the same set of labels, we define the *co-clusters* for each label as :

$$\Gamma_1 := \{(\mathbf{x}_i, \mathbf{y}_j) : q(\mathbf{x}_i) = r(\mathbf{y}_j) = 1\}, \quad \Gamma_2 := \{(\mathbf{x}_i, \mathbf{y}_j) : q(\mathbf{x}_i) = r(\mathbf{y}_j) = 2\}.$$

With small abuse of notation, we also write $\mathbf{x}_i \in \Gamma_z$ to indicate $q(\mathbf{x}_i) = z$, and likewise we write $\mathbf{y}_j \in \Gamma_z$ to indicate $r(\mathbf{y}_j) = z$. In terms of these co-clusters, the transport cost is:

$$\begin{aligned} \langle \mathbf{C}, \mathbf{Q}(1/\mathbf{g})\mathbf{R}^T \rangle &= \sum_{i=1}^n \sum_{j=1}^n c(\mathbf{x}_i, \mathbf{y}_j) \sum_{z \in \{1,2\}} \mathbf{Q}_{iz}(1/\mathbf{g}_z)\mathbf{R}_{zj}^T \\ &= \sum_{i=1}^n \sum_{j=1}^n c(\mathbf{x}_i, \mathbf{y}_j) \left(\frac{1}{g_1} \mathbf{Q}_{i1} \mathbf{R}_{j1} + \frac{1}{g_2} \mathbf{Q}_{i2} \mathbf{R}_{j2} \right) \\ &= \sum_{i=1}^n \sum_{j=1}^n c(\mathbf{x}_i, \mathbf{y}_j) \left(\frac{1}{g_1} \delta_{(\mathbf{x}_i, \mathbf{y}_j) \in \Gamma_1} + \frac{1}{g_2} \delta_{(\mathbf{x}_i, \mathbf{y}_j) \in \Gamma_2} \right) \\ &= \left(\frac{1}{g_1} \sum_{(\mathbf{x}_i, \mathbf{y}_j) \in \Gamma_1} c(\mathbf{x}_i, \mathbf{y}_j) + \frac{1}{g_2} \sum_{(\mathbf{x}_i, \mathbf{y}_j) \in \Gamma_2} c(\mathbf{x}_i, \mathbf{y}_j) \right), \end{aligned} \tag{S2}$$

where we have left in the uniform vector \mathbf{g} for clarity. Having assumed the existence of Monge map T , we lose no generality using it to index the second dataset: we suppose \mathbf{Y} is indexed so that $\mathbf{y}_i = T(\mathbf{x}_i)$. Note that, by optimality of T , one has for any permutation of the indices $\tau : [n] \rightarrow [n]$

$$\sum_{j=1}^n c(\mathbf{x}_i, T(\mathbf{x}_i)) \leq \sum_{j=1}^n c(\mathbf{x}_i, T(\mathbf{x}_{\tau(i)})). \tag{S3}$$

Returning to the low-rank cost function, suppose for the sake of contradiction that one has a pair $(\mathbf{x}_i, T(\mathbf{x}_i))$ neither contained in Γ_1 nor in Γ_2 . Again, without loss of generality, we may index this pair as $(\mathbf{x}_1, T(\mathbf{x}_1))$. To see that we may

assume that $\mathbf{x}_1 \in \Gamma_1$ but $T(\mathbf{x}_1) \in \Gamma_2$, note that n is assumed even, so the existence of such a pair symmetrically implies there is another $\mathbf{x} \in X$ with $\mathbf{x} \in \Gamma_2$ but $T(\mathbf{x}) \in \Gamma_1$. We lose no generality indexing this second pair as $(\mathbf{x}_2, T(\mathbf{x}_2))$. From the pairs $(\mathbf{x}_1, T(\mathbf{x}_1))$ and $(\mathbf{x}_2, T(\mathbf{x}_2))$, we build a new cluster assignment function $\tilde{q} : X \rightarrow \{1, 2\}$ as follows:

$$\tilde{q}(\mathbf{x}_i) = \begin{cases} 2 & \text{if } i = 1 \\ 1 & \text{if } i = 2 \\ q(\mathbf{x}_i) & \text{if } i \geq 3 \end{cases},$$

from which matrix $\tilde{\mathbf{Q}}$ is defined as above:

$$\tilde{\mathbf{Q}}_{iz} = \begin{cases} \frac{1}{n} & \text{if } \tilde{q}(\mathbf{x}_i) = z \\ 0 & \text{otherwise} \end{cases}.$$

Note that the cluster populations of $\tilde{\mathbf{Q}}$ coincide with those of \mathbf{Q} , thus $\tilde{\mathbf{Q}} \in \Pi(\mathbf{a}, \mathbf{g})$. Define $\mathbf{P}^* := \mathbf{Q} \text{diag}(1/\mathbf{g}) \mathbf{R}^T$, and define $\tilde{\mathbf{P}} := \tilde{\mathbf{Q}} \text{diag}(1/\mathbf{g}) \mathbf{R}^T$. Define the new co-clusters associated to $\tilde{\mathbf{P}}$ as:

$$\tilde{\Gamma}_1 := \{(\mathbf{x}_i, T(\mathbf{x}_j)) : \tilde{q}(\mathbf{x}_i) = r(T(\mathbf{x}_j)) = 1\}, \quad \tilde{\Gamma}_2 := \{(\mathbf{x}_i, T(\mathbf{x}_j)) : \tilde{q}(\mathbf{x}_i) = r(T(\mathbf{x}_j)) = 2\}.$$

Then, from (S2) one may write the transport cost of \mathbf{P}^* as:

$$\langle \mathbf{C}, \mathbf{P}^* \rangle = \left(\frac{1}{g_1} \sum_{(\mathbf{x}_i, \mathbf{y}_j) \in \Gamma_1} c(\mathbf{x}_i, \mathbf{y}_j) + \frac{1}{g_2} \sum_{(\mathbf{x}_i, \mathbf{y}_j) \in \Gamma_2} c(\mathbf{x}_i, \mathbf{y}_j) \right), \quad (\text{S4})$$

and likewise (S2) implies

$$\langle \mathbf{C}, \tilde{\mathbf{P}} \rangle = \left(\frac{1}{g_1} \sum_{(\mathbf{x}_i, \mathbf{y}_j) \in \tilde{\Gamma}_1} c(\mathbf{x}_i, \mathbf{y}_j) + \frac{1}{g_2} \sum_{(\mathbf{x}_i, \mathbf{y}_j) \in \tilde{\Gamma}_2} c(\mathbf{x}_i, \mathbf{y}_j) \right). \quad (\text{S5})$$

Subtracting (S5) from (S4), one has:

$$\langle \mathbf{C}, \mathbf{P}^* \rangle - \langle \mathbf{C}, \tilde{\mathbf{P}} \rangle = \frac{1}{g_1} (c(\mathbf{x}_1, T(\mathbf{x}_2)) - c(\mathbf{x}_1, T(\mathbf{x}_1))) + \frac{1}{g_2} (c(\mathbf{x}_2, T(\mathbf{x}_1)) - c(\mathbf{x}_2, T(\mathbf{x}_2))).$$

We now use that \mathbf{g} is uniform. From the last line above, (S3) implies that

$$\begin{aligned} &= 2 (c(\mathbf{x}_1, T(\mathbf{x}_2)) - c(\mathbf{x}_1, T(\mathbf{x}_1)) + c(\mathbf{x}_2, T(\mathbf{x}_1)) - c(\mathbf{x}_2, T(\mathbf{x}_2))) \\ &= 2 ([c(\mathbf{x}_1, T(\mathbf{x}_2)) + c(\mathbf{x}_2, T(\mathbf{x}_1))] - [c(\mathbf{x}_1, T(\mathbf{x}_1)) + c(\mathbf{x}_2, T(\mathbf{x}_2))]), \end{aligned}$$

where by adding and subtracting the non-permuted indices $\sum_{i \geq 3} c(\mathbf{x}_i, T(\mathbf{x}_i))$ and defining the permutation τ by \tilde{q} implies the cyclical monotonicity condition (Equation S3). Thus, we find

$$\begin{aligned} &= 2 \left(\sum_{i=1}^n c(\mathbf{x}_i, T(\mathbf{x}_{\tau(i)})) - \sum_{i=1}^n c(\mathbf{x}_i, T(\mathbf{x}_i)) \right) \geq 0, \\ &\implies \langle \mathbf{C}, \mathbf{P}^* \rangle_F \geq \langle \mathbf{C}, \tilde{\mathbf{P}} \rangle_F, \end{aligned}$$

assuming all (upper-triangular) values of the cost matrix are distinct the above inequality becomes strict, contradicting our assumption that \mathbf{P}^* was optimal. \square

Proposition B.3 (Refinement up to rank $r = 1$ produces tuples $(x, T(x))$ corresponding to the optimal permutation assuming a black-box optimal low-rank solver.).

Proof. Using Proposition B, this follows directly by induction on the rank $r = 2$ sub-divisions. For the base case of n points sub-divided into two co-clustered sets $\Gamma_1 = (\mathsf{X}^{(1)}, \mathsf{Y}^{(1)})$ of sizes

$$|\mathsf{X}^{(1)}| = |\mathsf{Y}^{(1)}| = \frac{n}{2}.$$

Proposition B implies that the Monge-map image is co-clustered with $\mathsf{X}^{(1)}$ as $T(\mathsf{X}^{(1)}) = \mathsf{Y}^{(1)}$. Likewise, the sets generated as $(\mathsf{X}^{(t)}, \mathsf{Y}^{(t)})$ from Γ_{t-1} maintain the invariant, so the inductive hypothesis holds at all levels up to singleton sets of the form $\Gamma_\tau = (x, T(x))$. \square

At each intermediate scale $t \in [\kappa]$, the *rank-schedule* (r_1, \dots, r_κ) determines the effective rank of the plan computed so far. For each $t \in [\kappa]$, define the *effective rank* at scale t as:

$$\rho_t := \prod_{s=1}^t r_s. \quad (\text{S6})$$

This effective rank is also the size of the partitions at scale t : $\rho_t = |\mathsf{X}^{(t)}| = |\mathsf{Y}^{(t)}|$, which are placed in bijective correspondence

$$\mathsf{X}_q^{(t)} \leftrightarrow \mathsf{Y}_q^{(t)} \quad t \in [\rho_t]. \quad (\text{S7})$$

at the t -th step of HiRef. We call ρ_t the effective rank because (to avoid quadratic space complexity) we never instantiate the transport plan corresponding to the bijective mapping (S7) as a matrix $\mathbf{T}^{(t)}$. Were we to instantiate $\mathbf{T}^{(t)}$, it would have rank ρ_t , and moreover we can evaluate its transport cost by using $\mathbf{T}^{(t)}$ to induce a transport plan $\mathbf{P}^{(t)}$ between the full datasets X, Y .

$$\mathbf{P}_{ij}^{(t)} := \begin{cases} \rho_t/n^2 & \text{if } q(n/\rho_t) < i, j \leq (q+1)(n/\rho_t) \\ 0 & \text{otherwise} \end{cases}, \quad (\text{S8})$$

where $q \in [\rho_t]$, and where the mass ρ_t/n^2 is a simplified form of $(\rho_t/n)^2(1/\rho_t)$. We note that this is a rewriting of $\frac{\rho_t}{n^2} \sum_{q=1}^{\rho_t} \delta_{(\mathbf{x}_i, \mathbf{y}_j) \in \Gamma_{t,q}}$ to have the indices ordered into a contiguous block-structure. Using plan (S8), which again we never instantiate, one can define:

$$\text{cost}(\mathbf{T}^{(t)}) := \langle \mathbf{C}, \mathbf{P}^{(t)} \rangle.$$

The next proposition shows that the costs $\langle \mathbf{C}, \mathbf{P}^{(t)} \rangle$ decrease as t increases from 1 to κ , and also provides a bound on their consecutive differences. Below, recall that each Γ_t denotes the co-clustering $(\mathsf{X}^{(t)}, \mathsf{Y}^{(t)})$, where

$$\mathsf{X}^{(t)} = \{\mathsf{X}_q^{(t)}\}_{q=1}^{\rho_t}, \quad \mathsf{Y}^{(t)} = \{\mathsf{Y}_q^{(t)}\}_{q=1}^{\rho_t},$$

and where co-cluster $\Gamma_{t,q}$ is defined as:

$$\Gamma_{t,q} := \{(\mathbf{x}, \mathbf{y}) : \mathbf{x} \in \mathsf{X}_q^{(t)}, \mathbf{y} \in \mathsf{Y}_q^{(t)}\}.$$

Proposition B.4 (Proposition 3.3). *Let cost c have the properties assumed at the beginning of the section, and let $\mathbf{P}^{(t)}$ be as defined above in (S8). Then one has the following bound on the difference in cost between iterations of refinement:*

$$0 \leq \langle \mathbf{C}, \mathbf{P}^{(t)} \rangle - \langle \mathbf{C}, \mathbf{P}^{(t+1)} \rangle \leq \|\nabla c\|_\infty \frac{1}{\rho_t} \sum_{q=1}^{\rho_t} \text{diam}(\Gamma_{t,q}), \quad (\text{S9})$$

where

$$\text{diam}(\Gamma_{t,q}) \equiv \text{diam}(\mathsf{X}_q^{(t)} \cup T(\mathsf{X}_q^{(t)})) := \max_{\mathbf{x}_i, \mathbf{x}_j, \mathbf{x}_k, \mathbf{x}_l \in \mathsf{X}_q^{(t)}} \left\| (\mathbf{x}_i, T(\mathbf{x}_j)) - (\mathbf{x}_k, T(\mathbf{x}_l)) \right\|.$$

Proof. By definition (S8) of $\mathbf{P}^{(t)}$,

$$\begin{aligned} \langle \mathbf{C}, \mathbf{P}^{(t)} \rangle - \langle \mathbf{C}, \mathbf{P}^{(t+1)} \rangle &= \frac{\rho_t}{n^2} \sum_{i=1}^n \sum_{j=1}^n c(\mathbf{x}_i, \mathbf{y}_j) \sum_{q=1}^{\rho_t} \delta_{(\mathbf{x}_i, \mathbf{y}_j) \in \Gamma_{t,q}} - \frac{\rho_{t+1}}{n^2} \sum_{i=1}^n \sum_{j=1}^n c(x_i, y_j) \sum_{q=1}^{\rho_{t+1}} \delta_{(\mathbf{x}_i, \mathbf{y}_j) \in \Gamma_{t+1,q}} \\ &= \frac{\rho_t}{n^2} \left(\sum_{i=1}^n \sum_{j=1}^n c(\mathbf{x}_i, \mathbf{y}_j) \sum_{q=1}^{\rho_t} \delta_{(\mathbf{x}_i, \mathbf{y}_j) \in \Gamma_{t,q}} - r_{t+1} \sum_{i=1}^n \sum_{j=1}^n c(\mathbf{x}_i, \mathbf{y}_j) \sum_{q'=1}^{\rho_{t+1}} \delta_{(\mathbf{x}_i, \mathbf{y}_j) \in \Gamma_{t+1,q'}} \right) \\ &= \frac{\rho_t}{n^2} \left(\sum_{q=1}^{\rho_t} \sum_{i=1}^n \sum_{j=1}^n c(\mathbf{x}_i, \mathbf{y}_j) \delta_{(\mathbf{x}_i, \mathbf{y}_j) \in \Gamma_{t,q}} - r_{t+1} \sum_{q'=1}^{\rho_{t+1}} \sum_{i=1}^n \sum_{j=1}^n c(\mathbf{x}_i, \mathbf{y}_j) \delta_{(\mathbf{x}_i, \mathbf{y}_j) \in \Gamma_{t+1,q'}} \right). \end{aligned}$$

By Proposition B, one then has:

$$= \frac{\rho_{t+1}}{n^2} \left(\sum_{q=1}^{\rho_t} \left(\underbrace{\frac{1}{r_{t+1}} \sum_{i \in X_q^{(t)}} \sum_{j \in X_q^{(t)}} c(\mathbf{x}_i, T(\mathbf{x}_j))}_{\text{average "Monge distortion" in } \Gamma_{t,q} \text{ over next scale}} - \underbrace{\sum_{z=1}^{r_{t+1}} \sum_{i \in X_{q\rho_{t+z}}^{(t+1)}} \sum_{j \in X_{q\rho_{t+z}}^{(t+1)}} c(\mathbf{x}_i, T(\mathbf{x}_j))}_{\text{"Monge distortion" at scale } t+1} \right) \right) \quad (\text{S10})$$

Note that the inner summands of (S10) (indexed by q) are non-negative by definition of the refinement step, where *within* each cluster, one has a minimization over a larger set of couplings. This shows $\langle \mathbf{C}, \mathbf{P}^{(t)} \rangle - \langle \mathbf{C}, \mathbf{P}^{(t+1)} \rangle \geq 0$. Towards an upper bound, we will bound each summand of (S10):

$$\left(\frac{1}{r_{t+1}} \sum_{i \in X_q^{(t)}} \sum_{j \in X_q^{(t)}} c(\mathbf{x}_i, T(\mathbf{x}_j)) - \sum_{z=1}^{r_{t+1}} \sum_{i \in X_{q\rho_{t+z}}^{(t+1)}} \sum_{j \in X_{q\rho_{t+z}}^{(t+1)}} c(\mathbf{x}_i, T(\mathbf{x}_j)) \right). \quad (\text{S11})$$

Define $s_{t+1} := n/\rho_{t+1}$ as well as barycenters

$$\bar{\mathbf{x}}^{(t)} := \sum_{\mathbf{x}_i \in X_{q\rho_{t+z}}^{(t+1)}} \frac{\mathbf{x}_i}{s_{t+1}}, \quad \bar{\mathbf{y}}^{(t)} := \sum_{\mathbf{x}_i \in X_{q\rho_{t+z}}^{(t+1)}} \frac{T(\mathbf{x}_i)}{s_{t+1}},$$

and note that by Jensen's inequality, for convex cost $c(\cdot, \cdot)$ one has:

$$\begin{aligned} \sum_{z=1}^{r_{t+1}} \sum_{\mathbf{x}_i \in X_{q\rho_{t+z}}^{(t+1)}} \sum_{\mathbf{x}_j \in X_{q\rho_{t+z}}^{(t+1)}} c(\mathbf{x}_i, T(\mathbf{x}_j)) &= s_{t+1}^2 \sum_{z=1}^{r_{t+1}} \sum_{\mathbf{x}_i \in X_{q\rho_{t+z}}^{(t+1)}} \frac{1}{s_{t+1}} \sum_{\mathbf{x}_j \in X_{q\rho_{t+z}}^{(t+1)}} \frac{1}{s_{t+1}} c(\mathbf{x}_i, T(\mathbf{x}_j)) \\ &\geq s_{t+1}^2 r_{t+1} c(\bar{\mathbf{x}}^{(t)}, \bar{\mathbf{y}}^{(t)}), \end{aligned}$$

so that we may continue upper-bounding the difference (S11):

$$\leq \frac{1}{r_{t+1}} \left(\sum_{\mathbf{x}_i \in X_q^{(t)}} \sum_{\mathbf{x}_j \in X_q^{(t)}} c(\mathbf{x}_i, T(\mathbf{x}_j)) \right) - s_{t+1}^2 r_{t+1} c(\bar{\mathbf{x}}^{(t)}, \bar{\mathbf{y}}^{(t)}) \quad (\text{S12})$$

$$= \frac{1}{r_{t+1}} \left(\left(\sum_{\mathbf{x}_i \in X_q^{(t)}} \sum_{\mathbf{x}_j \in X_q^{(t)}} c(\mathbf{x}_i, T(\mathbf{x}_j)) \right) - \frac{n^2}{\rho_t} c(\bar{\mathbf{x}}^{(t)}, \bar{\mathbf{y}}^{(t)}) \right) \quad (\text{S13})$$

$$= \frac{1}{r_{t+1}} \left(\sum_{\mathbf{x}_i \in X_q^{(t)}} \sum_{\mathbf{x}_j \in X_q^{(t)}} \left(c(\mathbf{x}_i, T(\mathbf{x}_j)) - c(\bar{\mathbf{x}}^{(t)}, \bar{\mathbf{y}}^{(t)}) \right) \right). \quad (\text{S14})$$

Now, define the diameter of co-cluster $\Gamma_{t,q}$ as follows:

$$\text{diam}(\Gamma_{t,q}) \equiv \text{diam}(\mathbf{X}_q^{(t)} \cup T(\mathbf{X}_q^{(t)})) := \max_{\mathbf{x}_i, \mathbf{x}_j, \mathbf{x}_k, \mathbf{x}_l \in \mathbf{X}_q^{(t)}} \left\| (\mathbf{x}_i, T(\mathbf{x}_j)) - (\mathbf{x}_k, T(\mathbf{x}_l)) \right\|,$$

Using our Lipschitz assumption on h made at the beginning of the section, where $c(\mathbf{x}, \mathbf{y}) = h(\mathbf{x} - \mathbf{y})$ (we will write $\|\nabla c\|_\infty$ for $\|\nabla h\|_\infty$), one has the inequality:

$$|c(\mathbf{x}_i, T(\mathbf{x}_i)) - c(\mathbf{x}_j, T(\mathbf{x}_j))| \leq \|\nabla c\|_\infty \text{diam}(\Gamma_{t,q}).$$

Thus, returning to the bound on each summand (S11), we obtain the upper bound:

$$\leq \frac{1}{r_{t+1}} \sum_{\mathbf{x}_i \in \mathbf{X}_q^{(t)}} \sum_{\mathbf{x}_j \in \mathbf{X}_q^{(t)}} \|\nabla c\|_\infty \left\| (\mathbf{x}_i, T(\mathbf{x}_j)) - (\bar{\mathbf{x}}^{(t)}, \bar{\mathbf{y}}^{(t)}) \right\| \quad (\text{S15})$$

As partition $\mathbf{X}^{(t+1)}$ is a refinement of $\mathbf{X}^{(t)}$ and $\mathbf{Y}^{(t+1)}$ is a refinement of $\mathbf{Y}^{(t)}$, it holds that (S11) is upper bounded by:

$$\leq \frac{1}{r_{t+1}} \sum_{i \in \mathbf{X}_q^{(t)}} \sum_{j \in \mathbf{X}_q^{(t)}} \|\nabla c\|_\infty \text{diam}(\Gamma_{t,q}), \quad (\text{S16})$$

$$= \frac{1}{r_{t+1}} |\mathbf{X}_q^{(t)}|^2 \|\nabla c\|_\infty \text{diam}(\Gamma_{t,q}), \quad (\text{S17})$$

$$= \frac{1}{r_{t+1}} \frac{n^2 \|\nabla c\|_\infty}{\rho_t^2} \text{diam}(\Gamma_{t,q}). \quad (\text{S18})$$

To conclude, we plug these bounds into each summand of (S10), obtaining the following bound on the full sum:

$$= \frac{\rho_{t+1}}{n^2} \frac{1}{r_{t+1}} \frac{n^2 \|\nabla c\|_\infty}{\rho_t^2} \sum_{q=1}^{\rho_t} \text{diam}(\Gamma_{t,q}) \quad (\text{S19})$$

$$= \|\nabla c\|_\infty \frac{1}{\rho_t} \sum_{q=1}^{\rho_t} \text{diam}(\Gamma_{t,q}). \quad (\text{S20})$$

completing the proof. \square

Remark B.5. Proposition B.4 should be considered a *conditional* result. Our proof follows that of (Proposition 1, (Gerber & Maggioni, 2017)), but they are able to provide sharper bounds between elements of a cluster and the centroid of the cluster using the properties assumed to hold in their definition of a multiscale family of partitions (Definition C.3), which mimic the structure of dyadic cubes in Euclidean space. As we do not make any geometric assumptions of our partitions, the above result is a priori weaker, through we leave the exploration of the geometry of partitions induced by low-rank OT to future work.

Remark B.6. Note, if $c(\mathbf{x}_i, T(\mathbf{x}_j)) = \gamma$ is constant (i.e., if all points are equidistant in a block), one has that refinement offers no gain from level $\Gamma_t \rightarrow \Gamma_{t+1}$:

$$\leq \frac{\rho_{t+1}}{n^2} \sum_{q=1}^{\rho_t} \left| \gamma \frac{|\mathbf{X}_q^{(t)}|^2}{r_{t+1}} - \gamma r_{t+1} |\mathbf{X}_q^{(t+1)}|^2 \right| = \frac{\rho_{t+1}}{n^2} \sum_{q=1}^{\rho_t} \left| \gamma \frac{(n/\rho_t)^2}{r_{t+1}} - \gamma r_{t+1} (n/\rho_{t+1})^2 \right| = 0.$$

Remark B.7. The work (Seguy et al., 2018) suggests a loss dependent on an (entropic) coupling γ . If γ is sparse and supported on the graph of the Monge map so that $\gamma = (\text{id} \times T)_\# \mu$, this loss becomes a regression of a neural network T_θ on the Monge map T over the support of μ : $\min_{T_\theta} \mathbb{E}_\mu c(T_\theta(\mathbf{x}_i), T(\mathbf{x}_i))$. Thus, as a bijective coupling can be represented as $\gamma = (\text{id} \times T)_\# \mu$, unlike an entropic one such an objective allows one to learn a neural map T_θ by directly matching T over the dataset support.

Proof. Via linearity of the push-forward

$$\begin{aligned} &= \int_{\mathbf{X} \times \mathbf{Y}} \|T_\theta(\mathbf{x}) - \mathbf{y}\|_2^p \left((\text{id} \times T)_\# \sum_{i=1}^n \mu_i \delta_{\mathbf{x}_i} \right) d\mathbf{x}d\mathbf{y} = \int_{\mathbf{X} \times \mathbf{Y}} \|T_\theta(\mathbf{x}) - \mathbf{y}\|_2^p \left(\sum_{i=1}^n \mu_i (\text{id} \times T)_\# \delta_{\mathbf{x}_i} \right) d\mathbf{x}d\mathbf{y} \\ &= \sum_{i=1}^n \mu_i \int_{\mathbf{X} \times \mathbf{Y}} \|T_\theta(\mathbf{x}) - \mathbf{y}\|_2^p \delta_{(\mathbf{x}_i, T(\mathbf{x}_i))} d\mathbf{y}d\mathbf{x} = \sum_{i=1}^n \mu_i \|T_\theta(\mathbf{x}_i) - T(\mathbf{x}_i)\|_2^p, \end{aligned}$$

By integrating against the δ . As $\mu_i > 0$, it holds that this loss is identically zero if and only if $T_\theta = T$ on the dataset $(\mathbf{x}_i)_{i=1}^n$

$$\min_{T_\theta} \int_{\mathbf{X} \times \mathbf{Y}} \|T_\theta(\mathbf{x}) - \mathbf{y}\|_2^p d\gamma(\mathbf{x}, \mathbf{y}) = 0 \iff \|T_\theta(\mathbf{x}_i) - T(\mathbf{x}_i)\|_2^p = 0 \iff T_\theta(\mathbf{x}_i) = T(\mathbf{x}_i)$$

□

C. Background: Multiscale Optimal Transport

C.1. Multiscale Partitions

(Gerber & Maggioni, 2017) describe a general multiscale strategy for computing OT plans between metric measure spaces (\mathbf{X}, d_X, μ) and (\mathbf{Y}, d_Y, ν) . They state this in the Kantorovich setting, using a general cost function $c : \mathbf{X} \times \mathbf{Y} \rightarrow \mathbb{R}_+$. Their framework consists of several elements:

1. A way of *coarsening* the set of source points \mathbf{X} and the measure μ across multiple scales:

$$(\mathbf{X}, \mu) =: (\mathbf{X}_J, \mu_J) \rightarrow (\mathbf{X}_{J-1}, \mu_{J-1}) \rightarrow \cdots \rightarrow (\mathbf{X}_1, \mu_1), \quad (\text{S21})$$

as well as an analogous coarsening for the set of target points \mathbf{Y} :

$$(\mathbf{Y}, \nu) =: (\mathbf{Y}_J, \nu_J) \rightarrow (\mathbf{Y}_{J-1}, \nu_{J-1}) \rightarrow \cdots \rightarrow (\mathbf{Y}_1, \nu_1), \quad (\text{S22})$$

where at each scale j , $\text{supp}(\mu_j) = \mathbf{X}_j$ and $\text{supp}(\nu_j) = \mathbf{Y}_j$, and the cardinality of each \mathbf{X}_j and \mathbf{Y}_j decreases with j .

2. A way of *propagating* coupling π_j solving the transport problem $\mu_j \rightarrow \nu_j$ at scale j to a coupling π_{j+1} at scale $j+1$.
3. A way of *refining the plan* from scale j to an optimal solution at scale $j+1$.

To derive approximation bounds for the error incurred by the multiscale transport problem at each scale, (Gerber & Maggioni, 2017) use regular families of multiscale partitions (Definition C.3 below) to define approximations to μ, ν and c at all scales.

For $z \in \mathbf{X}$, define $B_x(r) := \{x' \in \mathbf{X} : d_X(x, x') < r\}$ as the metric ball of radius r centered at x . Functions $f, g : \mathbf{X} \rightarrow \mathbb{R}$ have the *same order of magnitude* if there is $c_1, c_2 > 0$ with $c_1 f(x) \leq g(x) \leq c_2 f(x)$ for all $x \in \mathbf{X}$, and in this case we write $f \asymp g$. Write $\mathcal{M}(\mathbf{X})$ for the space of unsigned measures on \mathbf{X} , and write $\mathcal{P}(\mathbf{X})$ for the subspace of probability measures.

Definition C.1. A metric space (\mathbf{X}, d_X) has *doubling dimension* $d > 0$ if every $B_z(r)$ admits a covering by at most 2^d balls of radius $r/2$.

A metric space is said to be *doubling* if it has doubling dimension d for some $d > 0$. A related notion to a doubling metric space is a doubling measure.

Definition C.2. Measure $\mu \in \mathcal{M}(\mathbf{X})$ is a *doubling measure with dimension* d if there is a constant $c_1 > 0$ such that for all $x \in \mathbf{X}$ and all $r > 0$, one has $c_1^{-1} r^d \leq \mu(B_x(r)) \leq c_1 r^d$, i.e. $\mu(B_x(r)) \asymp r^d$.

Note that if (\mathbf{X}, d_X, μ) is doubling, then d_X is doubling, and up to modification of d_X to an equivalent metric, the dimension d can be taken as the same in either case.

Definition C.3. Given metric measure space (\mathbf{X}, d_X, μ) , a *regular family of multiscale partitions* with scaling parameter $\theta > 1$ is a family of sets

$$\left\{ \{C_{j,k}\}_{k=1}^{K_j} \right\}_{j=1}^J,$$

with each $C_{j,k} \subset \mathbf{X}$ such that:

1. For each scale j , the sets $\{C_{j,k}\}_{k=1}^{K_j}$ partition X .
2. For each scale $j \in [J-1]$, either $C_{j+1,k'} \cap C_{j,k} = \emptyset$ or $C_{j+1,k'} \subset C_{j,k}$. In this latter case, we say that $(j+1, k')$ is a *child* of (j, k) , or equivalently that (j, k) is a *parent* of $(j+1, k')$, writing $(j+1, k') \prec (j, k)$.
3. There is a constant $A > 0$ such that for all j, k , we have diameter $\text{diam}(C_{j,k}) \leq A\theta^{-j}$.
4. Each $C_{j,k}$ contains a ‘‘center point’’ $c_{j,k}$ such that $B_{c_{j,k}}(\theta^{-j}) \subset C_{j,k}$.

We take $\theta = 2$ for simplicity. As the child-parent terminology suggests, these partitions (through the second point) have a tree structure, like dyadic cubes in \mathbb{R}^d . Though the measure μ is not explicitly used in the above definition, the third and fourth points imply $\mu(C_{j,k}) \asymp 2^{-jd}$ and $K_j \asymp 2^{jd}$.

Coarsening spaces and measures Now suppose that each of X and Y are each discrete metric measure spaces, each equipped with regular families $\Gamma(X), \Gamma(Y)$ of multiscale partitions:

$$\begin{aligned} \Gamma(X) &:= \{\Gamma_j(X)\}_{j=0}^J, & \Gamma_j(X) &:= \{C_{j,k}(X)\}_{k=1}^{K_j(X)} \\ \Gamma(Y) &:= \{\Gamma_j(Y)\}_{j=0}^J, & \Gamma_j(Y) &:= \{C_{j,k}(Y)\}_{k=1}^{K_j(Y)}, \end{aligned}$$

and these yield the coarsening chains in (S21), (S22) in the most natural way possible at each scale j , defining the coarse-grained spaces X_j, Y_j to be the clusters at scale j :

$$X_j := \Gamma_j(X), \quad Y_j := \Gamma_j(Y),$$

while the measures at scale j are defined from the measures at scale $j+1$ via:

$$\mu_j(C_{j,k}(X)) := \sum_{(j+1,k') \prec (j,k)} \mu_{j+1}(C_{j+1,k'}(X)), \quad \nu_j(C_{j,k}(Y)) := \sum_{(j+1,k') \prec (j,k)} \nu_{j+1}(C_{j+1,k'}(Y)).$$

The fourth item of Definition C.3 requires that we define cluster centers $\bar{c}_{j,k}(X)$ for each $C_{j,k}(X)$. At the finest scale $j = J$, all clusters $C_{J,k}(X)$ correspond to singletons $\{x_{J,k}\}$, so we define $\bar{c}_{J,k}(X) := x_{J,k}$ in this case. At coarser scales, these centers can be defined recursively from the next finest scale, depending on the structure of X .

For example, if X has vector space structure (in addition to being a metric measure space), a natural choice for cluster centers $x_{j,k}$ at scale $j = 0, \dots, J-1$ is the weighted average $x_{j,k} := \bar{c}_{j,k}(X)$, where

$$\bar{c}_{j,k}(X) := \sum_{(j+1,k') \prec (j,k)} \mu_{j+1}(C_{j+1,k'}(X)) x_{j+1,k'}.$$

On the other hand, in the absence of vector space structure, one can still define

$$\bar{c}_{j,k}(X) = \arg \min_{x \in X} \sum_{(j+1,k') \prec (j,k)} d_X^p(x, x_{j+1,k'}),$$

with analogous constructions for Y yielding centers $y_{j,k}$.

Coarsening the cost function (Gerber & Maggioni, 2017) suggest three ways to coarsen the cost function using the multiscale partition. To condense the notation slightly, let us write $x_{j,k}$ in place of $C_{j,k}(X)$ and $y_{j,k'}$ in place of $C_{j,k}(X)$ and $C_{j,k'}(Y)$.

(c-i) The pointwise value

$$c_j(x_{j,k}, y_{j,k'}) := c(x_{j,k}, y_{j,k'}), \tag{S23}$$

using centers $x_{j,k}$ and $y_{j,k'}$ defined in any of the ways above.

(c-ii) The local average

$$c_j(x_{j,k}, y_{j,k'}) := \frac{\sum_{x \in C_{j,k}(X), y \in C_{j,k'}(Y)} c(x, y)}{|C_{j,k}(X)| |C_{j,k'}(Y)|}$$

(c-iii) The local weighted average:

$$c_j(x_{j,k}, y_{j,k'}) := \frac{\sum_{x \in C_{j,k}(X), y \in C_{j,k'}(Y)} c(x, y) \pi_{j-1}^*(x_{j-1,k_1}, y_{j-1,k'_1})}{\sum_{x \in C_{j,k}(X), y \in C_{j,k'}(Y)} \pi_{j-1}^*(x_{j-1,k_1}, y_{j-1,k'_1})},$$

where π_{j-1}^* is the optimal (or approximately optimal) OT plan at scale $j-1$, defined below. The indices k_1 and k'_1 are defined using the tree structure of the partition: k_1 is the unique index among $[K_{j-1}(X)]$ such that $(j, k) \prec (j-1, k_1)$, and likewise k'_1 is unique among $[K_{j-1}(Y)]$.

C.2. Propagation of OT solutions across scales

For each scale j , consider the OT problem given as follows.

$$\begin{aligned} \pi_j^* &:= \arg \min_{\pi \in \Pi(\mu_j, \nu_j)} \text{cost}(\pi), \quad \text{where:} \\ \text{cost}(\pi_j) &:= \sum_{k \in [K_j(X)], k' \in [K_j(Y)]} c(x_{j,k}, y_{j,k'}) \pi_j(x_{j,k}, y_{j,k'}) \end{aligned} \quad (\text{S24})$$

(Gerber & Maggioni, 2017) show bounds on $|\text{cost}(\pi_j^*) - \text{cost}(\pi_{j-1}^*)|$ of a constant times $2^{-j} \|\nabla c\|_\infty$, but note that this only implies closeness of the transport plans in terms of their cost, not necessarily in any other sense.

Given an optimal plan π_j^* at scale j , (Glimm & Henscheid, 2013) proposed a direct propagation strategy to initialize the problem at scale $j+1$, distributing the mass $\pi_j^*(x_{j,k}, y_{j,k'})$ equally to all combinations of paths between children $(x_{j,k})$ and children $(y_{j,k'})$. In this context, a path is understood to mean a source-target pair at the next scale, e.g. a pair of the form $(x_{j+1,\ell}, y_{j+1,\ell'})$. To formalize this, let

$$\mathcal{A}_j := \{(x_{j,k}, y_{j,k'}) : k \in [K_j(X)], k' \in [K_j(Y)]\}$$

denote *all* paths between points in X_j and Y_j . The drawback of this warm-start procedure is that if $\text{supp}(\mu_j) \subset \mathcal{A}_j$, which is always the case, the refinement procedure still requires quadratic space complexity at the finest scale.

To mitigate the ultimate quadratic space complexity of retaining all possible paths at all scales, (Gerber & Maggioni, 2017) allow for a refinement procedure where the support of transport plans at scale $j+1$ is restricted to a subset $\mathcal{R}_{j+1} \subset \mathcal{A}_{j+1}$ of all possible paths (with \mathcal{R}_{j+1} defined by the optimal plan at the previous iteration). Given $\mathcal{R}_j \subset \mathcal{A}_j$, let $\pi_j^*|_{\mathcal{R}_j}$ denote the optimal solution to the path-restricted or *restricted problem* at scale j :

$$\pi_j^*|_{\mathcal{R}_j} := \arg \min_{\substack{\pi \in \Pi(\mu_j, \nu_j), \\ \text{supp}(\pi) \subset \mathcal{R}_j}} \text{cost}(\pi). \quad (\text{S25})$$

Simple propagation. The simplest way to restrict the number of paths considered at subsequent scales is to use paths at scale j whose endpoints are children of mass-bearing paths at scale $j+1$:

$$\mathcal{R}_{j+1} := \{(x_{j+1,\ell}, y_{j+1,\ell'}) : \exists (x_{j,k}, y_{j,k'}) \in \text{supp}(\pi_j^*) \text{ s.t. } (j+1, \ell) \prec (j, k) \text{ and } (j+1, \ell') \prec (j, k')\}.$$

The optimal Kantorovich plan at scale j has at most $(K_j(X) + K_j(Y) + 1)$ non-zero entries. Using the above simple propagation strategy constrains plan at scale $j+1$ to be supported on at most

$$\alpha_j^2 (K_j(X) + K_j(Y))$$

entries, where α_j is the maximum number of children of any (j, k) across both datasets. When the ambient space has doubling dimension d , for any j one has $\alpha_j \asymp 2^d$, yielding a plan with *linear* space complexity at the finest scale.

Capacity constraint propagation. This propagation strategy solves a modified minimum flow problem at scale j in order to include additional paths at scale $j + 1$ likely to be included in the optimal solution π_{j+1}^* . Concretely, one first computes an unconstrained optimal plan $\pi_j^*|_{\mathcal{R}_j}$ at scale j . Then, a new OT plan $\tilde{\pi}_j^*|_{\mathcal{R}_j}$ is solved for at scale j now subject to the capacity constraint

$$\tilde{\pi}_j^*|_{\mathcal{R}_j} \leq U_{k,k'} \min(\mu(x_{j,k}), \nu(y_{j,k'}))$$

for each $(x_{j,k}, y_{j,k'}) \in \text{supp}(\pi_j^*|_{\mathcal{R}_j})$, where the random variables $U_{k,k'}$ are i.i.d. Uniform($[0.1, 0.9]$). This can also be iterated several times, in all cases leading to linear space complexity in the optimization at the finest scale.

C.3. Refinement of the propagated solution

Propagation of a solution to the restricted transport problem (S25) at scale j , in general cannot guarantee reaching an optimal solution to the restricted problem at scale $j + 1$, and can lead to accumulation of errors across all scales. Several *refinement* strategies are proposed in (Gerber & Maggioni, 2017) to address this.

Potential Refinement. One refinement strategy leverages the problem dual to (3), here stated at the finest scale:

$$\max_{\substack{\mathbf{f} \in \mathbb{R}^n, \mathbf{g} \in \mathbb{R}^m \\ \mathbf{f}_i + \mathbf{g}_j \leq \mathbf{C}_{ij}}} \sum_{i=1}^n \mu(\{x_i\}) \mathbf{f}_i + \sum_{j=1}^m \mu(\{y_j\}) \mathbf{g}_j. \quad (\text{S26})$$

The refinement strategy uses optimal dual variables $\mathbf{f}^*, \mathbf{g}^*$ to select paths to include at the next scale. From the dual formulation, an optimal solution $(\mathbf{f}^*, \mathbf{g}^*)$ to (S26) must have all nonnegative entries in the *reduced cost matrix*, defined as the matrix $\mathbf{C} - \mathbf{f} \oplus \mathbf{g}$ with entries $\mathbf{C}_{kk'} - \mathbf{f}_k - \mathbf{g}_{k'}$. Note that the dual to the restricted problem (S25) is well-defined, and for this dual we denote the optimal dual potentials by $\mathbf{f}^*|_{\mathcal{R}_j}$ and $\mathbf{g}^*|_{\mathcal{R}_j}$. With slight abuse of notation, let $(\mathbf{f}^* \oplus \mathbf{g}^*)|_{\mathcal{R}_j}$ be

$$(\mathbf{f}^* \oplus \mathbf{g}^*)|_{\mathcal{R}_j} := (\mathbf{f}^*|_{\mathcal{R}_j} \oplus \mathbf{g}^*|_{\mathcal{R}_j}) \odot \mathbf{M}^{(j)},$$

where $\mathbf{M}^{(j)}$ is the indicator matrix of the restricted set of paths \mathcal{R}_j at scale j , and where \odot denotes the Hadamard (entrywise) product. While the restricted set of paths \mathcal{R}_j is inherited from the previous scale, one can define a new set of paths \mathcal{V}_j^0 based on where the restricted reduced cost $\mathbf{C} - (\mathbf{f}^* \oplus \mathbf{g}^*)|_{\mathcal{R}_j}$ is nonpositive:

$$\mathcal{V}_j^0(\pi_j^*|_{\mathcal{R}_j}) := \{(x_{j,k}, y_{j,k'}) \in \mathcal{A}_j : \mathbf{C}_{kk'} - [(\mathbf{f}^* \oplus \mathbf{g}^*)|_{\mathcal{R}_j}]_{kk'} \leq 0\}.$$

With a new set of paths $\mathcal{Q}_j^0 := \mathcal{V}_j^0(\pi_j^*|_{\mathcal{R}_j})$, one can compute a new optimal plan $\pi_j^*|_{\mathcal{Q}_j^0}$ at scale j restricted to these paths, as well as *new* optimal dual potentials $\mathbf{f}^*|_{\mathcal{V}_j^0}$ and $\mathbf{g}^*|_{\mathcal{V}_j^0}$ leading to a new reduced cost $\mathbf{C} - (\mathbf{f}^* \oplus \mathbf{g}^*)|_{\mathcal{V}_j^0}$. This strategy can be iterated via

$$\mathcal{Q}_j^i := \mathcal{V}_j(\pi_j^*|_{\mathcal{Q}_j^{i-1}}), \quad (\text{S27})$$

yielding the sequence of transport plans $\pi_j^*|_{\mathcal{Q}_j^i}$, all at scale j , which converge on a solution whose reduced cost is nonnegative, necessarily making it optimal. The potential refinement strategy was used by (Glimm & Henscheid, 2013), with (Schmitzer, 2016) introducing shielding neighborhoods in a similar spirit, using dual potentials to locally verify global optimality.

D. Experimental Details

D.1. Synthetic Experiments

For all of the synthetic experiments, we first generate $n = 1024$ points from three datasets: the checkerboard dataset ((Makkuva et al., 2020)), the MAFMoons and Rings dataset ((Buzun et al., 2024)), and the Half-moon and S-curve dataset ((Buzun et al., 2024)). Following (Buzun et al., 2024) the random seed was set to 0 for data-generation with `jax.random.key(0)`. We evaluate the OT cost $\langle \mathbf{C}, \mathbf{P} \rangle_F$ of HiRef Sinkhorn (Cuturi, 2013), and ProgOT (Kassraie et al., 2024) on each of these three datasets, where we use (1) the Euclidean cost $\|\cdot\|_2$, and (2) the squared Euclidean cost $\|\cdot\|_2^2$ (Table S2). We additionally quantify the number of non-zero entries in the plan and its entropy (Table S3).

Checkerboard

Table S1. Hyperparameters for Synthetic Experiments

Parameter Name	Variable	Value
Rank-Annealing Schedule	(r_1, \dots, r_κ)	[2, 512]
Hierarchy Depth	κ	2
Maximal Base Rank	Q	2^{10}
Maximal Intermediate Rank	C	16

The checkerboard dataset (Makkuva et al., 2020) is defined by random variables $Y \sim Q$ sampled from the source distribution according to $\mathbf{Y} = \mathbf{X} + \mathbf{Z}$ where \mathbf{X} and \mathbf{Z} are sampled from Uniform distributions defined by

$$\begin{aligned} \mathbf{X} &\sim \text{Uniform}(\{(0, 0), (1, 1), (1, -1), (-1, 1), (-1, -1)\}), \\ \mathbf{Z} &\sim \text{Uniform}([-0.5, 0.5] \times [-0.5, 0.5]). \end{aligned}$$

the target distribution P has random variable \mathbf{Y}' where the random variable \mathbf{Y}' is defined as $\mathbf{Y}' = \mathbf{X}' + \mathbf{Z}$ with components

$$\begin{aligned} \mathbf{X}' &\sim \text{Uniform}(\{(0, 1), (0, -1), (1, 0), (-1, 0)\}), \\ \mathbf{Z} &\sim \text{Uniform}([-0.5, 0.5] \times [-0.5, 0.5]). \end{aligned}$$

MAFMoons and Rings

The MAFMoon dataset (Buzun et al., 2024) defines a source distribution Q by sampling $\mathbf{X} \sim \mathcal{N}(0, \mathbb{1}_2)$ and applying the non-linear transformation defined by

$$\mathbf{Y} = \begin{bmatrix} Y_1 \\ Y_2 \end{bmatrix} = \begin{bmatrix} 0.5(X_1 + X_2^2) - 5 \\ X_2 \end{bmatrix}$$

this introduces a quadratic dependency on the Gaussian randomly variable to generate a crescent shape.

The target distribution P representing concentric rings is generated by first sampling $\theta \sim \text{Uniform}(2\pi)$, with fixed radii $r_i \in \{0.25, 0.55, 0.9, 1.2\}$ from which one transforms to Cartesian coordinates as $x_i = 3r_i \cos \theta_i$ and $y_i = 3r_i \sin \theta_i$. Gaussian noise is added to each of these, as $\epsilon \sim \mathcal{N}(0, \mathbb{1}\sigma^2)$ for $\sigma = 0.08$.

Half-moon and S-Curve

The Half-moon and S-curve dataset (Buzun et al., 2024) is generated from $\mathbf{Y} = \text{make_moons}$ and make_S_curve from the `scikit-learn` library. Both datasets are transformed further with a rotation $\mathbf{R}(\theta)$, a scaling λ , and a translation μ applied as $\mathbf{Y}' \leftarrow \mathbf{R}(\theta)(\lambda\mathbf{Y}) + \mu$.

 Table S2. Comparison Table for Coupling-Based OT Methods on Primal Cost $\langle \mathbf{C}, \mathbf{P} \rangle_F$ for $\|\cdot\|_2$ and $\|\cdot\|_2^2$

Method	Checkerboard (Makkuva 2020)		MAFMoons & Rings (Buzun 2024)		Half Moon & S-Curve (Buzun 2024)	
	$\ \cdot\ _2$	$\ \cdot\ _2^2$	$\ \cdot\ _2$	$\ \cdot\ _2^2$	$\ \cdot\ _2$	$\ \cdot\ _2^2$
Sinkhorn	0.3573	0.1319	0.4422	0.4440	0.5663	0.5663
ProgOT	N/A	0.1320	N/A	0.4443	N/A	0.5709
HiRef	0.3533	0.1248	0.4398	0.4414	0.5741	0.5737

 Table S3. Entropy and Non-Zero Entries ($> 10^{-8}$) of Coupling Matrices for Each Method and Dataset (Wasserstein-2 distance cost, $\|\cdot\|_2^2$)

Method	Checkerboard (Makkuva 2020)		MAFMoons & Rings (Buzun 2024)		Half Moon & S-Curve (Buzun 2024)	
	Entropy	Non-Zeros	Entropy	Non-Zeros	Entropy	Non-Zeros
Sinkhorn	12.8509	624733	12.6117	678720	12.7776	652993
ProgOT	12.3830	271087	11.6158	327764	12.1170	337258
HiRef	6.9314	1024	6.9314	1024	6.9314	1024

Table S4. Comparison of Coupling-Based OT Methods on Primal Cost $\langle C, P \rangle_F$ (Wasserstein-2) on 512 point small instance.

Method	Checkerboard	MAF Moons & Rings	Half Moon & S-Curve
Sinkhorn (<code>ott-jax</code>)	0.136	0.221	0.338
ProgOT	0.136	0.216	0.334
HiRef	0.129	0.216	0.334
Dual Revised Simplex Solver	0.127	0.214	0.332

Table S5. Hyperparameters for Mouse-Embryo Spatial Transcriptomics Experiment (E15.5-16.5)

Parameter Name	Variable	Value
Rank-Annealing Schedule	(r_1, \dots, r_κ)	[2, 86, 659]
Hierarchy Depth	κ	3
Maximal Base Rank	Q	2^{10}
Maximal Intermediate Rank	C	128

D.2. Large-scale Transcriptomics Matching on Mouse-Embryo

In this problem, we use HiRef to find a full-rank alignment matrix between successive pairs of spatial transcriptomics (ST) (Stahl et al., 2016) slices. These are from a dataset of whole-mouse embryogenesis (Chen et al., 2022) on the Stereo-Seq platform. These datasets have been measured at successive 1-day time-intervals: E9.5 ($n = 5913$), E10.5 ($n = 18408$), E11.5 ($n = 30124$), E12.5 ($n = 51365$), E13.5 ($n = 77369$), E14.5 ($n = 102519$), E15.5 ($n = 113350$), and E16.5 ($n = 121767$), where the embryonic mouse is growing across the stages so that the sample-complexity n increases with the numeric stage. For each pair of datasets of size n and m , we sub-sample the datasets so that the size of the two datasets is given as $n \leftarrow \min\{n, m\}$.

In the context of spatial transcriptomics, an experiment conducted on a two-dimensional tissue slice produces a data pair (\mathbf{X}, \mathbf{Z}) . Here, $\mathbf{X} \in \mathbb{R}^{n \times p}$ represents the gene expression matrix, where n denotes the number of cells (or spatial spots) analyzed on the slice, and p signifies the number of genes measured. Specifically, the entry $\mathbf{X}_{ij} \in \mathbb{R}_+$ corresponds to the expression level of gene j in cell i , with higher values indicating greater expression intensity. Concurrently, $\mathbf{Z} \in \mathbb{R}^{n \times 2}$ is the spatial coordinate matrix, where each row i contains the (x, y) coordinates of cell i on the tissue slice. Consequently, every cell on the slice is characterized by a gene expression vector of length p , capturing its molecular features, and a coordinate vector of length two, detailing its spatial position within the slice.

We utilize the extensive, real-world dataset on mouse embryo development presented in (Chen et al., 2022), which encompasses eight temporal snapshots of spatial transcriptomics (ST) slices throughout the entire mouse embryo development process. And align all consecutive timepoints. The preprocessing of this dataset is conducted using the standard SCANPY (Wolf et al., 2018) workflow. Initially, we ensure that both slices contain an identical set of genes by filtering, which results in a common gene set across all cells for each pair of timepoints. Subsequently, we apply log-normalization to the gene expression data of all cells from the two slices. To compress the data, we perform Principal Component Analysis (PCA), reducing the dimensionality of the gene expression profiles to $d = 60$ PCs. Finally, we compute the Euclidean distances between gene expression vectors in the PCA-transformed space to construct the cost matrix \mathbf{C} , on which we solve a Wasserstein problem to obtain the optimal coupling \mathbf{P} of full-rank. We offer hyperparameters for the E15-16.5 experiment (the largest alignment) in Table S5. For the other experiments, the maximal intermediate rank is $r = 16$ up to E10.5, $r = 32$ to E11.5, $r = 64$ up to E13.5, and 128 for E14.5-16.5. The rank-annealing schedule is generated according to the dynamic program in each case by the `rank_annealing.optimal_rank_schedule(n, hierarchy_depth, max_Q, max_rank)` function.

D.3. Brain Atlas Spatial Alignment

We took inspiration from MERFISH-MERFISH alignment experiments of (Clifton et al., 2023), particularly gene abundance transfer tasks that STalign is exhibited on. The data are available on the Vizgen website for MERFISH Mouse Brain Receptor Map data release (<https://info.vizgen.com/mouse-brain-map>). The two spatial transcriptomics slices used for the experiment are slice 2, replicate 3 (“source” dataset) and slice 2, replicate 2 (“target” dataset). The datasets will be denoted $(\mathbf{X}^1, \mathbf{S}^1)$ for the source and $(\mathbf{X}^2, \mathbf{S}^2)$ for the target.

Table S6. Cost Values $\langle \mathbf{P}, \mathbf{C} \rangle_F$ for Different Methods Across Embryonic Stages

Method	E9.5-E10.5	E10.5-E11.5	E11.5-E12.5	E12.5-E13.5	E13.5-E14.5	E14.5-E15.5	E15.5-E16.5
HiRef	21.8088	14.8126	16.1396	14.5741	13.7851	14.2901	12.7880
Sinkhorn	21.9137	14.8893	N/A	N/A	N/A	N/A	N/A
ProgOT	22.5607	15.3539	N/A	N/A	N/A	N/A	N/A
FRLC	23.1443	16.0926	17.7380	15.4707	14.6422	15.5055	14.0034

Table S7. Cosine Similarity Scores for Expression Transfer

Method	<i>Slc17a7</i>	<i>Grm4</i>	<i>Olig1</i>	<i>Gad1</i>	<i>Peg10</i>
HiRef (this work)	0.8098	0.7959	0.7526	0.4932	0.6015
FRLC (Halmos et al., 2024)	0.2098	0.2072	0.1756	0.0959	0.0692
LOT (Scetbon et al., 2021)	0.3241	0.2279	0.3029	0.1653	0.0719

The source dataset consists of 85,958 spots, while the target dataset consists of 84,172 spots. To apply HiRef to these data, we subsampled the source dataset to have 84,172 spots also (uniformly at random), removing a total of 1786 spots. We ran HiRef using the settings `max_rank = 11` and `hierarchy_depth=4`, for a total runtime of 10 minutes 6 seconds, on an A100 GPU. The random seed was set to 44. For the cost function used by HiRef, we only use the *spatial* modalities $\mathbf{S}^1, \mathbf{S}^2$ of the two datasets. We centered the spatial coordinates of both datasets, and applied a rotation by 45 degrees to the first dataset. With these registered spatial data, here denoted $\tilde{\mathbf{S}}^1 = \{\mathbf{s}_i^1\}_{i=1}^n$ and $\tilde{\mathbf{S}}^2 = \{\mathbf{s}_i^2\}_{i=1}^n$, we formed the cost matrix \mathbf{C} given by:

$$C_{ij} = \|\mathbf{s}_i^1 - \mathbf{s}_j^2\|_2,$$

where $\|\cdot\|_2$ denotes the Euclidean distance between the spatial coordinates. This cost \mathbf{C} was used as input to HiRef, which produced as output a 1-1 mapping T between the two datasets (a permutation matrix is too large to instantiate).

We then evaluated the performance of HiRef through cosine similarity of predicted gene abundance with target gene abundance, across five ‘‘spatially-patterned’’ genes: *Slc17a7*, *Grm4*, *Olig1*, *Gad1*, *Peg10*. Writing g to stand in for any of these genes, we formed the abundance vectors $\mathbf{v}^{1,g}$ and $\mathbf{v}^{2,g}$ using the raw counts for gene g in each datasets’ expression component $\mathbf{X}^1, \mathbf{X}^2$. Using HiRef output T , we also formed the *predicted* abundance vector $\hat{\mathbf{v}}^g$, which maps the raw counts from $\mathbf{v}^{1,g}$ to the spots in the second dataset through T .

Moreover, to compute cosine similarities between predicted and true expression abundances, (Clifton et al., 2023) employ a spatial binning on their output, using windows of $200\mu\text{m}$ to tile each slice. The diameter of each slice is roughly $10,000\mu\text{m}$, and to make our output comparable, we used the spatial coordinates \mathbf{S}' to bin and average the vectors $\mathbf{v}^{2,g}$ and $\hat{\mathbf{v}}$ locally. We used a total of 5625 bins, corresponding to a 15-to-1 mapping from spots to bins. Averaging the abundance of gene g in each bin, we obtain spatially smoothed versions of $\mathbf{v}^{2,g}$ and $\hat{\mathbf{v}}$, as in (Clifton et al., 2023). Denote these smoothed vectors by $\mathbf{w}^{2,g}$ and $\hat{\mathbf{w}}$. For each gene g among $\{Slc17a7, Grm4, Olig1, Gad1, Peg10\}$, we computed the cosine similarity between $\mathbf{w}^{2,g}$ and $\hat{\mathbf{w}}$, listing our results in Table S7. In the same table, we list scores obtained by the low-rank methods FRLC (Halmos et al., 2024) and LOT (Scetbon et al., 2021) for comparison. For the FRLC algorithm, we set $\alpha = 0$, $\gamma = 200$, $\tau_{\text{in}} = 500$, rank $r = 500$, using 200 outer iterations and 300 inner iterations. The runtime of FRLC was 9 minutes 57 seconds on an A100 GPU. We used as input a low-rank factorization of cost matrix \mathbf{C} , using the same rank $r = 500$ as for the transport plan itself. For the LOT algorithm, we were unable to pass a low-rank factorization of the distance matrix, so we had to use a smaller rank $r = 20$ in order to avoid exceeding GPU memory (the choice $r = 20$ led to memory usage of 30GB). We set $\epsilon = 0.01$ and otherwise used the default settings of the method. The total runtime was 44 minutes 39 seconds on an A100 GPU. To form a spot-to-spot mapping from each transport plan output by FRLC and LOT, we mapped the spot with index i in the first slice to the index argmax of the i -th row of the transport plan. We applied the exact same spatial averaging to the outputs of all methods. We plot the ground-truth and HiRef-predicted abundances in Figure S1.

D.4. Alignment of ImageNet Embeddings

To demonstrate the scalability of HiRef to massive and high-dimensional datasets, we perform an alignment unprecedented for OT solvers: aligning 1.2 million images from the ImageNet ILSVRC dataset (Russakovsky et al., 2015; Deng et al., 2009).

Table S8. Cost Values $\langle C, P \rangle_F$ for ImageNet (Russakovsky et al., 2015; Deng et al., 2009) Alignment Task.

Method	HiRef	Sinkhorn	ProgOT	FRLC	LOT
OT Cost	18.974	N/A	N/A	24.119	N/A

Table S9. Hyperparameters for ImageNet Experiment

Parameter Name	Variable	Value
Rank-Annealing Schedule	(r_1, \dots, r_κ)	[7, 50, 1830]
Hierarchy Depth	κ	3
Maximal Base Rank	Q	2^{11}
Maximal Intermediate Rank	C	64

A negligible amount of sub-sampling, on the order of ten points, was applied so that n divided into two integers which are not prime. We used the ResNet50 architecture (He et al., 2016) available at <https://download.pytorch.org/models/resnet50-0676ba61.pth> to generate embeddings of each image of dimension $d = 2048$. We then took a 50:50 split of the dataset as the two image datasets X, Y to be aligned, where we used a random permutation of the indices of the dataset using `torch.randperm` so that the splits approximately represent the same distribution over images. We then aligned these image datasets using HiRef and FRLC, with the final cost value shown in Table S8.

E. Additional Information

There are a number of additional practical details regarding Algorithm 1 in its actual implementation. In particular, to achieve linear scaling, one must also have sample-linear approximation of the distance matrix C . We use the algorithm of (Indyk et al., 2019) to accomplish this, as discussed in Section E.1. In addition, one requires parallel sequence of ranks for the distance matrices used at each step, (d_1, \dots, d_κ) . As a default, we set $(d_1, \dots, d_\kappa) = (r_1, \dots, r_\kappa)$ so that the ranks of the distance matrices parallel those of the coupling matrices. Moreover, HiRef has the capacity to be heavily parallelized: since Algorithm 1 breaks each instance into independent partitions, one may also parallelize the low-rank sub-problems of Algorithm 1 across compute nodes.

E.1. Optimizing the Rank-Annealing Schedule

As discussed in Section 3.3, the large constants required by low-rank OT (LR-OT) in practice encourage factorizations which have *minimal* partial sums. In particular, one seeks a factorization which minimizes the number of times LR-OT is run as a sub-procedure. Suppose one defines the maximal admissible rank of the low-rank solutions to be $C \in \mathbb{Z}_+$, the hierarchy-depth to be κ , the number of data-points to be n , and the maximal-rank permissible for the base-case alignment to be Q . If $Q \neq 1$, then one may take $n \leftarrow \frac{n}{Q}$, $\kappa \leftarrow \kappa - 1$, to observe that the total number of runs required is $1 + r_1 + r_1 r_2 + \dots + \prod_{i=1}^{\kappa} r_i \propto_{r_i} \left[\sum_{j=1}^{\kappa} \prod_{i=1}^j r_i \right]$, where the ranks factor the sample-size as $\prod_{i=1}^{\kappa} r_i = n$. Thus, to optimize the number of LR-OT calls for a given hierarchy-depth κ , one can optimize for the rank-annealing schedule by minimizing the sum of partial products defined by

$$\begin{aligned} \min_{(r_i)_{i=1}^{\kappa}} & \left[\sum_{j=1}^{\kappa} \prod_{i=1}^j r_i \right] \\ \text{s.t.} & \prod_{i=1}^{\kappa} r_i = n, \quad r_i \in \mathbb{Z}_+ \\ & r_i \leq C \end{aligned}$$

observing that $\min_{(r_i)_{i=1}^{\kappa}} \left[\sum_{j=1}^{\kappa} \prod_{i=1}^j r_i \right] = \min_{(r_i)_{i=1}^{\kappa}} \left[r_1 + r_1 \sum_{j=2}^{\kappa} \prod_{i=2}^j r_i \right]$ implies one may use a standard dynamic-programming approach and store a table of factors up to C to optimize this in $O(C\kappa n)$ time. Assuming κ, C are small constants, this implies that determining the rank-schedule is a simple linear-time procedure. The dynamic program accomplishing

this is implemented in the `rank_annealing` package by calling the `rank_annealing.optimal_rank_schedule(n, hierarchy_depth, max_Q, max_rank)` function. This depends on the number of data points n , the hierarchy depth κ , the maximal rank at the intermediate couplings Q , and the maximal rank to solve for the terminal coupling (r_{base}) `max_rank`.

Low-rank distance matrix \mathbf{C} . A key work (Indyk et al., 2019) showed that one may approximately factor a distance matrix \mathbf{C} with linear complexity in the number of points n (Algorithm E.1). For certain costs, e.g. squared Euclidean, this factorization can be given for free (Scetbon et al., 2021). We rely on both of these for low-rank factorizations of the distance matrix, so that both the space of the coupling and pairwise distance matrix scale linearly.

Algorithm 3 Low-Rank approximation for distance matrix \mathbf{C}

Input point sets $\{\mathbf{x}_i\}_{i=1}^n, \{\mathbf{y}_j\}_{j=1}^m$ in metric space \mathcal{X} and metric d
 Pick indices $i^* \in [n], j^* \in [m]$ uniformly at random
for $i = 1$ to n **do**
 Update sample probability $p_i = d(\mathbf{x}_i, \mathbf{y}_{j^*})^2 + d(\mathbf{x}_{i^*}, \mathbf{y}_{j^*})^2 + \frac{1}{m} \sum_{j=1}^m d(\mathbf{x}_{i^*}, \mathbf{y}_j)^2$
end for
 Sample $O(r/\varepsilon)$ rows $\mathbf{C}_{i,\cdot} \sim \text{Categorical}\left(\frac{p_i}{\sum_i p_i}\right)$
 Compute \mathbf{U} using (Frieze et al., 2004)
 Compute \mathbf{V} using (Chen & Price, 2017)
 return \mathbf{V}, \mathbf{U}

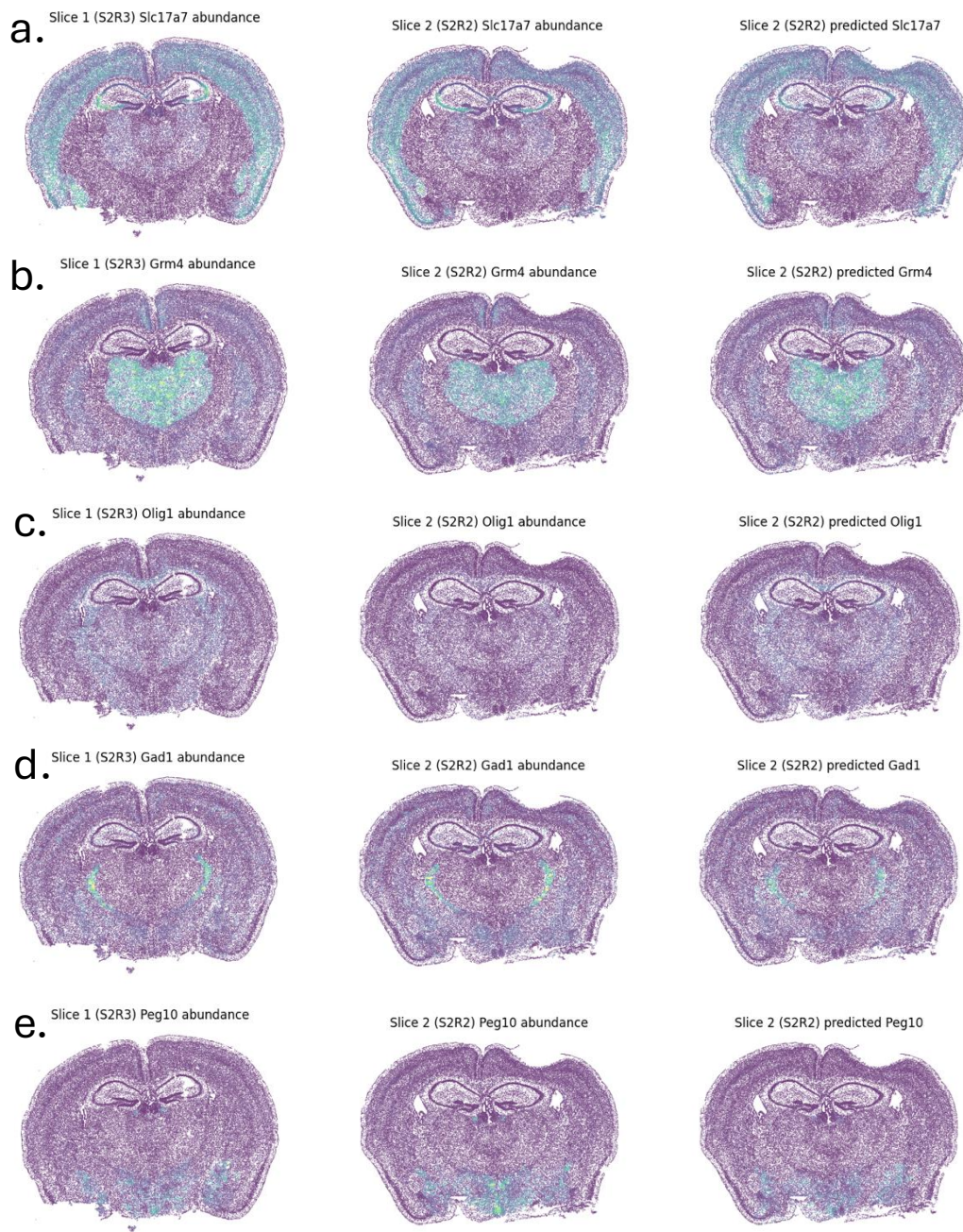


Figure S1. Abundance of 5 genes (a. *Slc17a7*, b. *Grm4*, c. *Olig1*, d. *Gad1*, e. *Peg10*) in Allen Brain Atlas MERFISH dataset (Clifton et al., 2023). From left to right are plotted (1) abundance in the first dataset, (2) abundance in the second dataset, and (3) predicted abundance via transfer of the abundances in the first dataset under the mapping of HiRef.

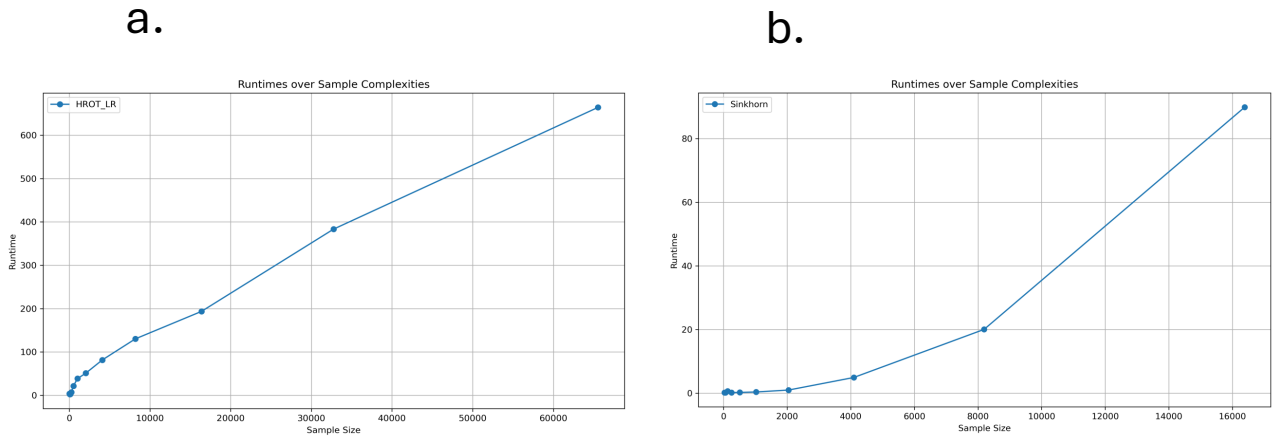


Figure S2. Runtime scaling with W_2^2 cost on 1 CPU core. **a.** HiRef runtime scales linearly with the problem instance, **b.** Sinkhorn runtime scales quadratically with the problem instance.

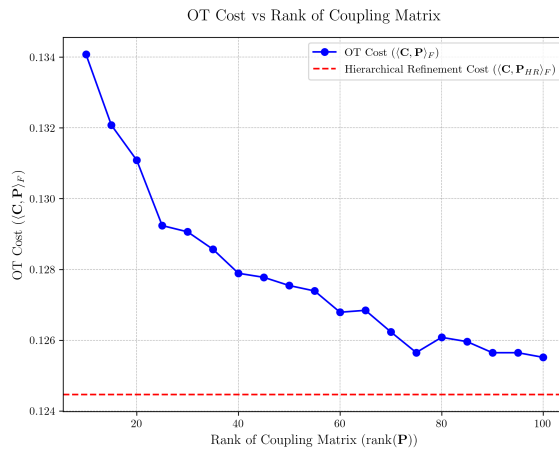


Figure S3. HiRef cost and the cost of the low-rank OT solution of FRLC (Halmos et al., 2024) across the coupling rank $r \in [5, 100]$.

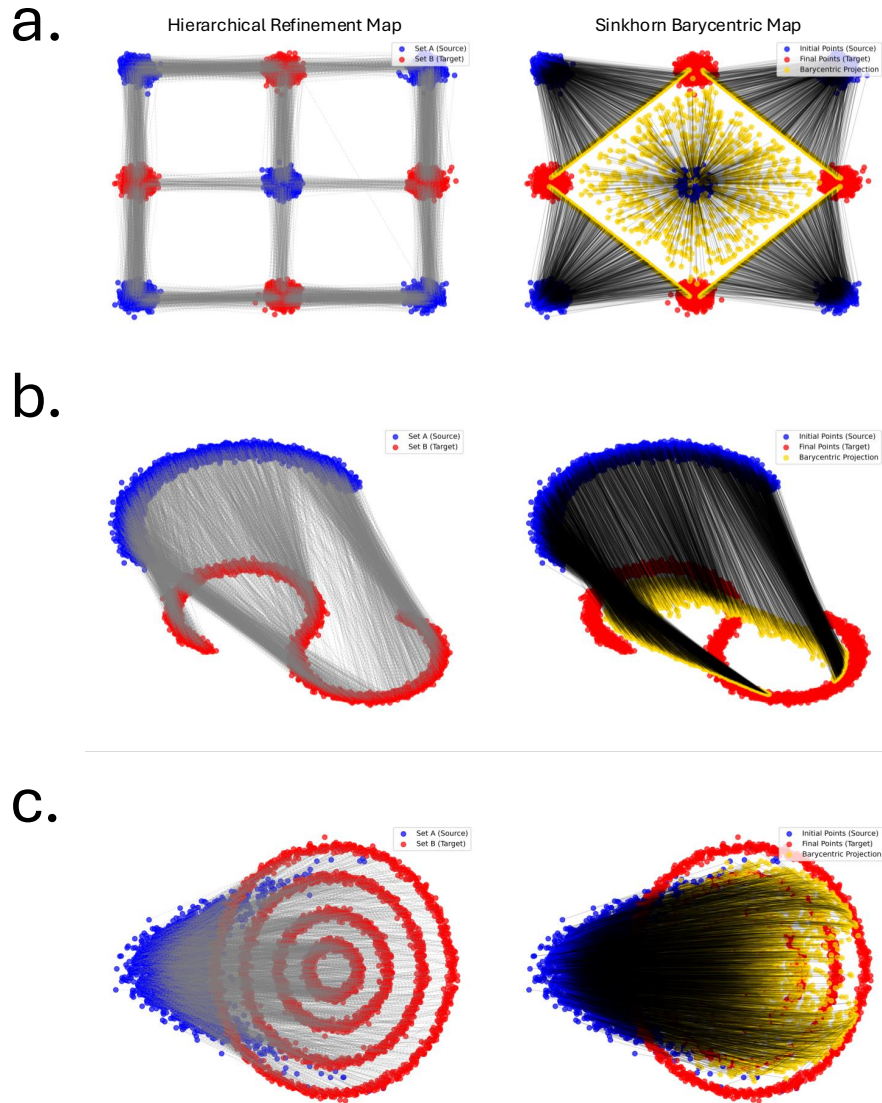


Figure S4. Comparison of optimal transport maps under (1) the HiRef alignment, and (2) the Sinkhorn (Cuturi, 2013) barycentric projection. **a.** The checkerboard dataset of (Makkuva et al., 2020), **b.** the Half-moon and S-curve dataset of (Buzun et al., 2024), and **c.** the MAF-Moons Rings dataset of (Buzun et al., 2024).

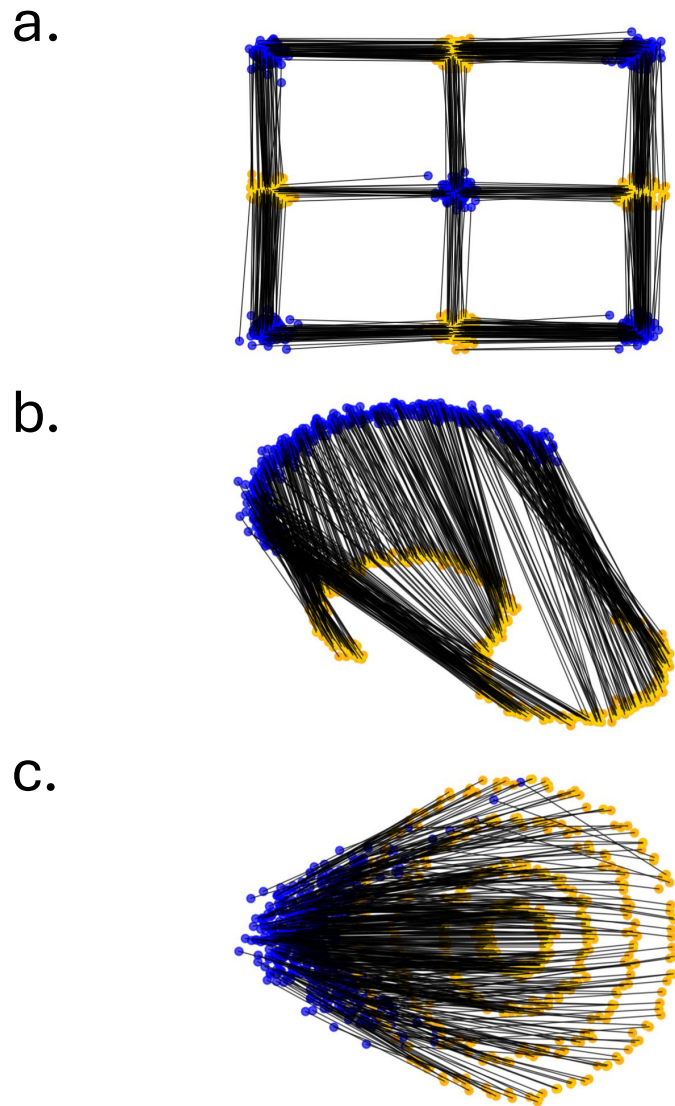


Figure S5. Alignments of the synthetic datasets of (Makkuva et al., 2020; Buzun et al., 2024) using the optimal dual revised simplex (Huangfu & Hall, 2017) algorithm for small instances (512 points). **a.** The checkerboard dataset of (Makkuva et al., 2020), **b.** the Half-moon and S-curve dataset of (Buzun et al., 2024), and **c.** the MAF-Moons Rings dataset of (Buzun et al., 2024).